Structure, redox states, and magnetic properties of $Li_{1-x}Ni_{1-z}Co_{z/2}Mn_{z/2}O_2$ cathode materials with $z = 1/5$, $2/5$, or $2/3$ at different states of charge x

Björn Schwarz [1,*] Stefan Mangold [2] Hang Li [1] Sylvio Indris [1] and Helmut Ehrenberg [1]

[1] Karlsruhe Institute of Technology (KIT), Institute for Applied Materials (IAM), 76344 Eggenstein-Leopoldshafen, Germany

[2] Karlsruhe Institute of Technology (KIT), Institute for Photon Science and Synchrotron Radiation (IPS), 76344 Eggenstein-Leopoldshafen, Germany

(Received 7 October 2024; revised 11 February 2025; accepted 27 March 2025; published 22 April 2025)

Cathode materials $Li_{1-x}Ni_{1-z}Co_{z/2}Mn_{z/2}O_2$ with $z = 1/5$ (NCM811), $z = 2/5$ (NCM622), or $z = 2/3$ (NCM111) in (i) the pristine state, (ii) charged to $x = 0.5$ or $x = 0.65$, and (iii) discharged after having been charged previously were characterized by x-ray diffraction (XRD), x-ray absorption spectroscopy (XAS), direct current (DC) and alternating current (AC) magnetometry, heat capacity, and nuclear magnetic resonance (NMR) spectroscopy. The magnetic properties of these layered oxides are decisively determined by Ni^{2+} ions that have migrated from the transition metal (TM) layer to the Li layer and that are magnetically coupled to the Ni, Co, or Mn cations occupying neighboring sites within the adjacent TM layers. For the pristine and discharged states, this cluster formation causes a bifurcation between the zero-field-cooled (ZFC) and the field-cooled (FC) susceptibility vs temperature curve (which sets in continuously below about 100 K) and is responsible for the appearance of a broad maximum of the imaginary χ'' susceptibility vs temperature curve that is centered around 14, 23, and 25 K for pristine NCM111, NCM622, and NCM811, respectively. The charged states with reduced Ni^{2+} amount do no longer show these features pointing to a strongly reduced cluster formation ability. Further, three-dimensional (frustrated) magnetic long-range ordering that leads to a broad local maximum in the heat capacity curve and to another abrupt bifurcation of the ZFC/FC susceptibility vs temperature curve (both observable slightly below 10 K) are additional features that all compositions (and states of charge) have in common. With increasing Ni to Co/Mn ratio, this low-temperature magnetic transition exhibits a more pronounced "partial" spin-glass-like characteristic as inferred from the frequency shift of the local AC susceptibility maximum. The results from AC/DC magnetometry and heat capacity measurements return complementary information to what can be inferred from XRD, XAS, and NMR investigations about the Ni to Co/Mn ratio, the Li/Ni disorder, and the TMs' oxidation states. The systematic investigation of samples with different Ni to Co/Mn ratios (going from NCM811 via NCM622 to NCM111) and with different oxidation states of the TMs (at different states of charge) allows for a better understanding of how the magnetic phenomena are correlated with the (real) structure and electronic properties in these layered oxide cathode materials.

DOI: 10.1103/PhysRevMaterials.9.045401

I. INTRODUCTION

Strong research activities have been undertaken during the last decades to develop lithium-ion batteries with high-energy density, good rate capability, and high stability [1–3]. The layered TM oxides Li(Ni, Co, Mn)O_2 (NCM) with trigonal α-$NaFeO_2$ structure type are still of high interest owing to their unique combination of properties [4–6]. In order to gain insight into structural details of these NCM cathode materials, especially in dependence on the Li content, also their magnetic properties have been investigated that contain valuable information about the TMs' oxidation states and their spatial distributions on crystallographic sites, for instance [7–18]. The magnetic properties of the end member $LiNiO_2$ have been investigated extensively, experimentally as well as theoretically, since it exhibits characteristics of a special model system [11,18–26]. Firstly, Anderson suggested that a resonating valence bond ground state may exist in a spin $S = 1/2$ Heisenberg triangular-lattice antiferromagnet [27,28], and Hirakawa *et al.* [29,30] proposed $LiNiO_2$ to be a potential physical realization of such a system. The second important feature is the peculiar electronic state of the Ni^{3+} ions that are brought into the low-spin state $(t_{2g})^6(e_g)^1$ by a strong crystal field, with the two e_g levels being degenerate [24]. The interplay between frustration on a triangular lattice [31] together with the orbital degeneracy, is supposed to decisively determine the magnetic properties of $LiNiO_2$ that are still not fully understood and remain the object of ongoing fundamental research.

A simplified phenomenological magnetic model has been reported by Chappel *et al.* [19], where hypothetical stoichiometric $LiNiO_2$, without any disorder between Li and Ni, could be characterized by a rather strong ferromagnetic (FM) intralayer coupling between the Ni in the TM layer and a

*Contact author: bjoern.schwarz@kit.edu

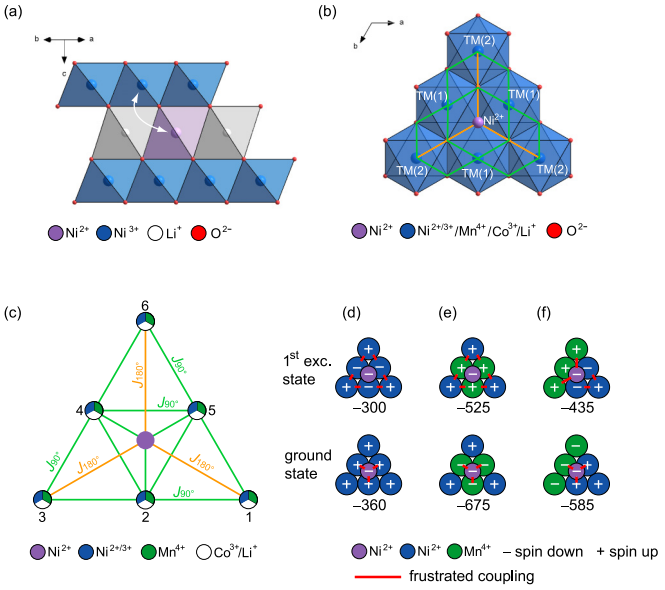

FIG. 1. Magnetic model. (a) Section of the alternating TM, Li, and TM layer sequence as present in quasistoichiometric $Li_{1-y}Ni_{1+y}O_2$ with small y value. The double arrow illustrates the exchange of a Li^+ ion from the Li layer with a Ni^{2+} ion from the TM layer. (b) Section of TM layer next to a Ni^{2+} that has migrated into the Li layer together with 90° (green) and 180° (orange) TM-O-TM magnetic super exchange paths. (c) More detailed illustration of what is shown in (b). (d)–(f) Magnetic energies (numbers) of ground state and first excited state calculated according to explanations given in Sec. S1 within the SM [38] (magnetic energy with the same unit as the isotropic exchange constants set equal one) for: (d) six Ni^{2+} in the TM layer, (e) three Ni^{2+} and three Mn^{4+} in the TM layer with a specific cationic arrangement, and (f) also three Ni^{2+} and three Mn^{4+}, but with another cationic arrangement.

comparably weak antiferromagnetic (AFM) interlayer coupling between Ni ions from adjacent TM layers, mediated via the Li layer. For quasi-stoichiometric $Li_{1-y}Ni_{1+y}O_2$ with small y value, generally a small amount (in the low single-digit percent regime) of Li from the Li layer has been exchanged by Ni^{2+} from the TM layer [see Fig. 1(a)]. The migrated Ni^{2+} in the Li layer is supposed to couple strongly AFM with Ni moments located in both adjacent TM layers, resulting in an effective FM coupling between the Ni moments in the direct vicinity to the interslab Ni^{2+}. Thereby, a small ferrimagnetic cluster is formed where the Ni moments in the TM layer are supposed to be in magnetic frustration with their direct Ni neighbors. For $y = 0.004$, the ZFC and FC susceptibility curves have been reported to exhibit a bifurcation below about 8 K, with the FC curve remaining approximately horizontal as typical for a spin-glass-like behavior [19]. For the just described $Li_{1-y}Ni_{1+y}O_2$ systems, a substitution of Li by Ni in the Li layer has been realized, whereas for the pristine $LiNi_{1-z}Co_{z/2}Mn_{z/2}O_2$ compounds that are subject of this paper, a 1.0 Li stoichiometry is preserved only allowing for a Li/Ni site exchange. Chernova *et al.* [11] investigated the magnetic properties of $Li_xNi_yMn_yCo_{1-2y}O_2$ cathodes that are closely related to the materials examined in this paper here. For simplicity, they only considered Ni^{2+}, Ni^{3+}, and Mn^{4+} to play a role for the magnetic coupling pathways in the pristine state of the material. Co was not considered explicitly in the first place, since it is assumed to be present exclusively as diamagnetic Co^{3+} (in octahedral crystal field) that does not actively mediate a magnetic coupling, but interrupts magnetic coupling paths. When a Ni^{2+} ion migrates to the Li layer by exchange with a Li ion in $Li_xNi_yMn_yCo_{1-2y}O_2$, various magnetic super exchange coupling paths have to be considered, as illustrated in Fig. 1(b). According to Chernova *et al.* [11], there exist three Ni^{2+}-O-TM(1) paths with an angle close to 90° (green lines), and three Ni^{2+}-O-TM(2) paths with an angle close to 180° (orange lines) that are coupled with the central Ni^{2+} ion that is located in the Li layer (purple). Further, all TMs within the TM layer are coupled with the nearest neighbor via 90° TM(1/2)-O-TM(1/2) coupling paths. Altogether this leads to the super exchange coupling scheme that is illustrated in Fig. 1(c) with the Ni^{2+} ion in the center (purple disk) and six cations in direct vicinity in the adjacent TM layer. According to Chernova *et al.* [11], the 180° Ni^{2+}-O-TM(1) couplings are reported to be very strong AFM for Ni^{2+}-O-Ni^{2+}, strong FM for Ni^{2+}-O-Mn^{4+}, and moderate AFM for Ni^{2+}-O-Ni^{3+}. For the 90° Ni^{2+}-O-TM(2) and the 90° TM(1/2)-O-TM(1/2), on the other side, the couplings are listed as strong AFM for Ni^{2+}-O-Mn^{4+}, moderate FM for Mn^{4+}-O-Mn^{4+}, and weak FM for Ni^{3+}-O-Ni^{3+}. The dependence of magnetic super exchange coupling on the geometry of local bonding and on the participating cations is described semiquantitatively by the Goodenough-Kanamori-Anderson rules [32–37].

This complex scheme of interconnected coupling paths together with the circumstance that the sign (FM or AFM) and strength of a certain superexchange path depend on the specific pair of TMs as well as on their oxidation states has specific consequences on how the composition and finally the specific cation arrangements affect the magnetic (ground) state energies and the degree of magnetic frustration around a Ni^{2+} that has migrated to the Li layer. In Sec. II, more revealing insights into how the magnetic properties of the layered oxide NCM materials depend on the local cationic arrangements will be presented by discussing three simple examples of cation arrangements.

In this paper, $Li_{1-x}Ni_{1-z}Co_{z/2}Mn_{z/2}O_2$ cathode materials with $z = 1/5$, $2/5$, or $2/3$ were investigated by powder XRD, synchrotron XAS, DC and AC magnetometry, heat capacity, and NMR spectroscopy for various states of charge x. The aim was to gain more insight into how structure, redox states of TMs, and physical/magnetic properties are correlated with each other in these layered oxide cathode materials.

II. MAGNETIC MODEL

A simple pseudospin $\tilde{S} = 1/2$ Ising-type magnetic model has been applied to the magnetic coupling scheme as shown in Fig. 1(c), to calculate the magnetic energy of the ground and the first excited state for three illustrative examples as described in detail in Sec. S1 within the Supplemental Material (SM) [38]. The magnetic model is strongly simplified by only considering a single adjacent TM layer next to the Ni^{2+} that has migrated to the Li layer. The magnetic coupling paths, qualitatively summarized from Ref. [11] already above, were quantified for the calculations according to the isotropic

exchange parameters J_{iso} listed in Table S1 within the SM [38].

Figure 1(d) presents the case in which the central Ni^{2+} (purple) that has migrated to the Li layer couples with six Ni^{2+} that are located in direct vicinity in the TM layer. In the ground state (GS), all Ni^{2+} are coupled FM with each other. A dominant FM coupling has also been found experimentally in this paper for the Ni-rich compounds in form of a positive Weiss constant. Even though there are only Ni^{2+} ions involved, the ground state is magnetically frustrated owing to the triangular lattice geometry and the peculiar values of the 90° and 180° Ni-O-Ni couplings. It can easily be imagined that the interslab Ni^{2+} finds another six Ni^{2+} located within the other adjacent TM layer to form a small ferrimagnetic cluster, as already mentioned above. Flipping three spin states of the GS creates the first excited state, whose energy is only slightly above that of the ground state owing to the weak 90° Ni-O-Ni FM couplings involved. Different spin orderings that are close in energy to each other more likely show spin-glass-like behavior, and indeed the magnetic transitions found for Ni-rich compounds in this paper exhibit spin-glass-like contributions.

Figures 1(e) and 1(f), present the case that the central Ni^{2+} couples with three Ni^{2+} and three Mn^{4+} that are located in direct vicinity of the TM layer, but with a different specific cation arrangement. The fact that the GS of the cation arrangement shown in Fig. 1(e) has a lower magnetic energy than that shown in Fig. 1(f), points to a correlation between cationic order and magnetic energy that has remarkable consequences. Zheng *et al.* [39], for example, have reported the role of super exchange on the Ni/Li disordering in layered $LiNi_xCo_yMn_zO_2$ and the magnetic frustration effect on the rate performance of $LiNi_{0.6}Co_{0.4-x}Mn_xO_2$ cathodes was revealed by Ye *et al.* [40]. For the ground states, the three Ni^{2+} are coupled FM with each other, and the three Mn^{4+} are coupled FM with each other, but the Ni^{2+} are coupled AFM to the Mn^{4+}. Since Mn^{4+} has a higher magnetic moment than Ni^{2+}, the total effective magnetic moment increases when Ni is substituted by Mn, but the net total magnetization of the ordered moments at low temperature becomes reduced owing to the AFM ordering between the Ni and Mn species. Also, the ferrimagnetic clusters possess a reduced magnetic net moment owing to the AFM ordering of Ni- and Mn-subunits within the TM layer. All these phenomena have also been observed experimentally in this paper and will be presented below. Moreover, a negative Weiss constant found for Mn-enriched compounds further correctly indicates the stronger contributions from the AFM 90° Ni-O-Mn couplings [41]. The first excited states for both of these cation arrangements are considerably higher than for the pure Ni-containing system, since the involved isotropic exchange parameters J_{iso} of the 90° Ni-O-Mn coupling paths are considerably stronger than the 90° Ni-O-Ni couplings. This is in agreement with what has been found in this paper experimentally as the magnetic order transitions of the Mn-richer compounds do not show spin-glass-like characteristics.

III. RESULTS AND DISCUSSION

A. Elemental composition

Active cathode materials of nominal composition $Li_{1-x}Ni_{1-z}Co_{z/2}Mn_{z/2}O_2$, with z being either 1/5, 2/5, or 2/3, were received from commercial manufacturers (see Table S2 within the SM [38] for details) in a fully lithiated pristine state with $x = 0$. The corresponding explicit nominal compositions $LiNi_{0.8}Co_{0.1}Mn_{0.1}O_2$ ($z = 1/5$), $LiNi_{0.6}Co_{0.2}Mn_{0.2}O_2$ ($z = 2/5$), and $LiNi_{0.33}Co_{0.33}Mn_{0.33}O_2$ ($z = 2/3$) will be named according to the common abbreviations NCM811, NCM622, and NCM111, respectively, in this paper. The elemental compositions of the samples have been determined experimentally by inductively coupled plasma optical emission spectroscopy (ICP-OES). Table S3 within the SM [38] lists the atomic concentrations c_n of Li, Ni, Co, Mn, and O with the sum of the TMs Ni, Co, and Mn normalized to one. Taking the errors of c_n into account (given in brackets), the samples' elemental compositions are well represented by the nominal stoichiometry according to NCM111, NCM622, and NCM811, respectively.

B. Electrochemistry and sample nomenclature

By electrochemical charging/discharging, Li can be extracted ($\Delta x > 0$)/inserted ($\Delta x < 0$) from/into the host structure with x defining the amount of delithiation. Electrodes consisting of 70 wt% active material (NCM111, NCM622, or NCM811), 20 wt% carbon black, and 10 wt% PTFE binder were electrochemically modified by galvanostatic charging/discharging at a current rate of $C_{th}/40$ (≈6.9 mA g^{-1}, with C_{th} being the theoretical capacity corresponding to full delithiation) in half cells against a Li metal anode (see Sec. S2 within the SM [38] for more details). A suffix following the samples' name indicates the type of electrochemical modification that the sample has undergone. The suffix "p" stands for pristine material ($x = 0$), "c50" for charged to $x = 0.5$ (≈139 mAh g^{-1}), "c65" for charged to $x = 0.65$ (≈180 mAh g^{-1}), "c50d" for charged to $x = 0.5$ and subsequently discharged to $E_w = 2.5$ V, and "c65d" for charged to $x = 0.65$ and subsequently discharged to $E_w = 2.5$ V. Following this nomenclature, NCM622-c50d, as an example, stands for a sample with composition $Li_{1-x}Ni_{0.6}Co_{0.2}Mn_{0.2}O_2$ that has first been charged to $x = 0.5$ (half delithiated) before it has been discharged (relithiated) until $E_w = 2.5$ V. Figures S1–S3 within the SM [38] present the electrochemical (EC) curves E_w vs x for all compositions and charging/discharging protocols. Table S4 within the SM [38] lists detailed information about the electrochemical modification, as for instance the irreversible first-cycle capacity loss for the c50d and c65d samples.

C. X-ray diffraction

Figures 2(a) and 2(b) exemplarily show the results of the Rietveld refinements [42] to the XRD patterns of NCM111-p and NCM111-c50, respectively (see Figs. S4–S6 within the SM [38] for a compilation of Rietveld refinements to the XRD patterns from all samples). For all samples, a single phase of the typical layered NCM oxide possessing a trigonal α-$NaFeO_2$ structure type (space group symmetry $R\bar{3}m$, no. 166 in International Tables for Crystallography [43]) has been used for the simulation of the patterns (see Sec. S2 within the SM [38] for details of the structural model). Figure 3 plots the refined lattice parameters c and a, the O-TM-O and

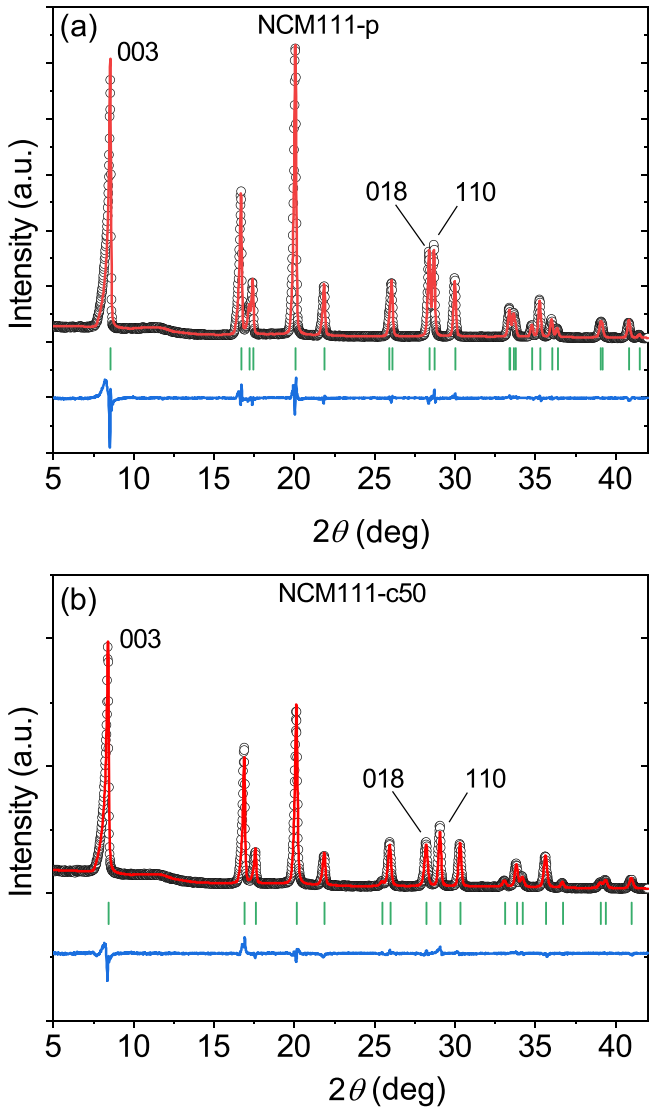

FIG. 2. Exemplarily, the results of the Rietveld refinement to the XRD pattern of (a) NCM111-p and (b) NCM111-c50 are presented (see SM [38] for results from all samples). Measured intensities (black circles), simulated intensities (red line), their difference curve (blue line), and the positions of the Bragg reflections (green ticks) for the layered NCM structure with $R\bar{3}m$ space group symmetry are shown.

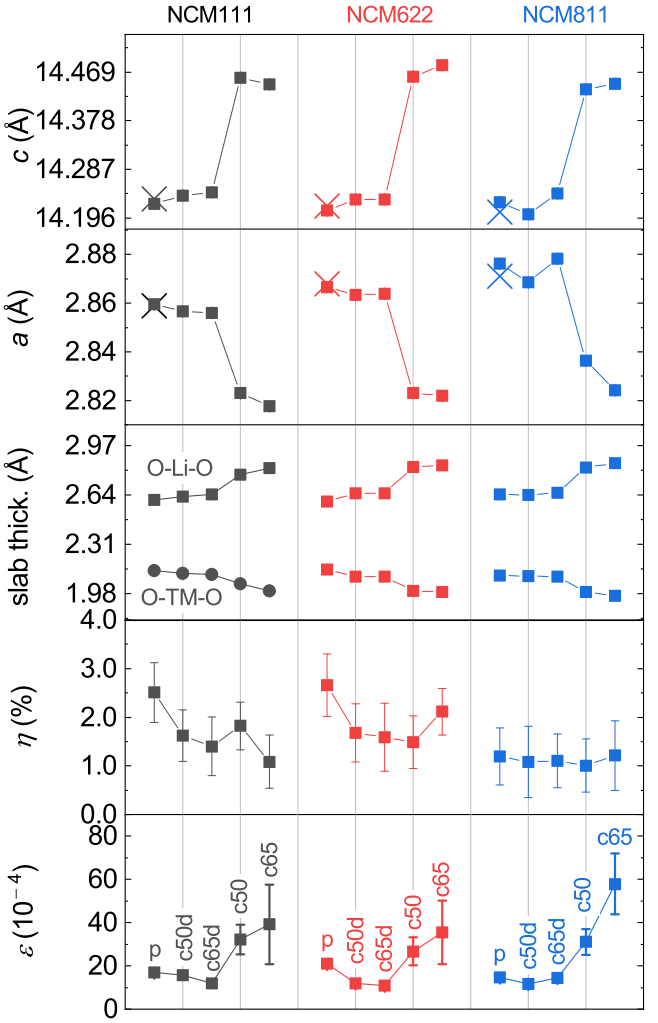

FIG. 3. Parameters as obtained by Rietveld refinement to the XRD patterns of all samples. Lattice parameter c and $a = b$, O-Li-O and O-TM-O slab thicknesses (estimated standard deviations smaller than symbols for lattice parameters and slab thicknesses), Li/Ni exchange η of Li from the Li layer with Ni from the TM layer, and strain ϵ (for charged samples, c50 and c65, values represent isotropic strain and error bars represent hexagonal anisotropic strain). Crosses are values published in Azhari *et al.* [44].

O-Li-O slab thicknesses, the Li/Ni disorder parameter η (relative occupation of TM layer by Li that has been exchanged with Ni), and the apparent lattice strain ϵ (for charged samples c50 and c65 the error bars represent anisotropic strain). Whereas the lattice parameter c approximately exhibits the same value for all compositions, lattice parameter a slightly increases in the order NCM111-p, NCM622-p, and NCM811-p for the pristine materials. This trend and also the absolute values, are in good agreement with those published in Ref. [44], for instance (values are inserted as crosses in Fig. 3).

In general, delithiation increases the average oxidation state of the TMs and causes a reduction of the average TM-O distances as long as no additional processes, such as low-spin to high-spin transitions, for instance, are involved simultaneously. For the NCMs, such a distance reduction is indeed realized by the evolution of lattice parameter a. Lattice parameter c initially increases with charging, because the extraction of Li^+ ions from the Li layer leads to a stronger repulsion of the negatively charged O anions from each other. At charge capacities of around 130 mAh g^{-1}, the c lattice parameter evolution becomes plateau-like, before c begins to decrease steeply again during further charging in a similar manner for NCM111, NCM622, and NCM811 as found by *operando* XRD analysis [45–47]. At high-charge capacities as those realized for $x = 0.65$ in this paper (corresponds to about 180 mAh g^{-1}), partial oxidation of oxygen contributes to charge compensation causing a strong decrease of the c lattice parameter. This oxygen contribution might firstly occur throughout the bulk (proposedly by local peroxide formation), but condensation of these partially oxidized oxygen species at the surface over time with subsequent irreversible oxy-

gen release and structural reconstructions at the surface are suggested [4,48–51]. The dependence of the measured lattice parameters a and c as well as that of the slab thicknesses on the SOC reflects mostly what is expected. The lattice parameter a monotonically decreases with charging and the c lattice parameter firstly increases with charging. From *operando* XRD analysis [45,46], a considerably smaller c lattice parameter would have been expected again for the c65 compared to the c50 state of charge, what cannot be observed experimentally here. Most probably, the above mentioned kinetic processes of oxygen oxidation play a stronger role for the here-applied *ex situ* XRD analysis and the bulk material has already partially relaxed for the highly charged c65 state, while the surface-near regions have been reconstructed instead. It is important to note that this "saturating" behavior, i.e., a nonlinear dependence on the delithiation x, cannot only be observed for the lattice parameters, but also for most of the investigated magnetic parameters for the highly charged c65 states as outlined below, reflecting the relaxation processes that have taken place in the hours after the electrochemical charging. On the other side, the refined anisotropic hexagonal strain, is found considerably larger for the c65 states than for the c50 states for NCM622 and NCM811 (see error bar evolution of the ϵ parameter) thereby indicating that the high charging (c65) leads to a high degree of lattice parameter variation that does not disappear over time. Another point of importance is the general trend that the values of the lattice parameters as well as those of the slab thicknesses for the discharged states c50d and c65d do not fully return back to their pristine values, indicating that subtle irreversible structural changes have occurred during charging. Those structural changes do not mean bulk phase transitions, but subtle modifications regarding cation ordering or reconstructions at the surface for instance. Thin surface layers of a spinel and/or a (Li containing) rock-salt phase are capable of affecting the Li ion transmissivity through the particle surface and contribute to reducing the total amount of Li that can be re-intercalated by discharging [4,48–51]. The Li/Ni disorder parameter η exhibits very similar values for NCM111-p and NCM622-p that are both slightly larger than that refined for NCM811-p. The site exchange of Li^+ from the Li layer with Ni^{2+} from the TM layer (both cations have very similar cation radii) is enhanced for NCM111-p (and NCM622-p) compared to NCM811-p, because the amount of Ni^{2+} increases with higher Mn to Ni ratio, as discussed in more detail below. For NCM111-p and NCM622-p, the average values of η exhibit a trend to become (irreversibly) smaller during charging/delithiation, but this trend cannot unambiguously be claimed to be present due to the comparably large standard deviations. The refined apparent strain parameter ϵ strongly increases as the degree of delithiation x increases from $x = 0$ (p), to $x = 0.5$ (c50) and further to $x = 0.65$ (c65). Simultaneously with the increase of the apparent strain, the hexagonal anisotropic strain, parameterized here as an additionally refinable variation σ_c of the c lattice parameter, also increases. The hexagonal anisotropy is represented by the error bars of the strain parameter in Fig. 3. Illustratively, the increasing strain owing to delithiation can be thought to be caused by a inhomogeneous distribution of the Li ions, either within single crystallites or potentially also from crystallite to crystallite (these two scenarios cannot be distinguished based on the available data). As a consequence of the varying Li content, the lattice parameters also exhibit a corresponding variation that is described as strain parameter ϵ. There are no clear indications that the strain parameter also exhibits any kind of irreversibility.

D. Magnetic and electronic properties

1. ZFC/FC susceptibility

Figure S7 within the SM [38] shows the ZFC/FC susceptibility vs temperature curves from 2–300 K for all compositions and for all states of charge. Figure 4 presents enlarged sections up to 50 K of the same data. From 300 K down to roughly about 100 K, the ZFC/FC curves mainly exhibit a Langevin-type paramagnetism of localized magnetic moments that obey the Curie-Weiss law,

$$\chi = \frac{C_c}{(T - \theta_{CW})}, \quad \text{or} \quad \chi^{-1} = C_c^{-1}(T - \theta_{CW}), \qquad (1)$$

with the Curie constant C_c, the Weiss constant θ_{CW}, and temperature T. The results of Curie-Weiss fits to the linear inverse susceptibility vs temperature curves from 100 to 300 K will be presented below. When the temperature is decreased below approximately 100 K, the formation of short-range ferrimagnetic clusters leads to a smooth and continuous increase of the susceptibility beyond what can be attributed to the Curie-Weiss behavior of the initially presented (uncoupled) magnetic moments. This deviation can most clearly be detected by the deviation from the pure linear progression of the inverse susceptibility χ^{-1} vs temperature curve that is realized at higher temperatures (see Fig. S8 within the SM [38]).

The formation of these ferrimagnetic clusters is connected with magnetic irreversibility (magnetic history dependence) that causes the ZFC and the FC susceptibility branches to bifurcate. Only the pristine and the discharged states c50d and c65d exhibit ZFC/FC bifurcations that smoothly set in below approximately 100 K (for temperatures <50 K these bifurcations can then clearly be observed), whereas the charged states c50 and c65 do not show such clear bifurcations for temperatures >10 K [see Figs. 4(a)–4(c)]. To quantify this observation, the difference areas $\Delta A_{FC/ZFC}$ between the ZFC and the FC susceptibility curves have been determined for temperatures >10 K and are plotted in Fig. 5(a). $\Delta A_{FC/ZFC}$ is much larger for the discharged than for the charged states, i.e., after charging the irreversibility owing to the cluster formation that sets in already below about 100 K is no longer present, in agreement with what has been found by the AC susceptibility investigations (see Sec. III D 6 below). Further, for NCM811, the absolute $\Delta A_{FC/ZFC}$ values are an order of magnitude larger than those for NCM111 or NCM622. Beside this continuous process of cluster formation that sets in already below approximately 100 K, another more abrupt phase transition slightly below 10 K can be observed that is characterized by a clear bifurcation of the ZFC and the FC curve and by a decreasing FC curve after a maximum susceptibility has been reached at temperature T_{FC}^{max} (that is also called blocking temperature T_b in the case of a spin freezing). Figure 5(b) plots the temperatures of local maxima of the FC curves T_{FC}^{max}. These values are a measure for the strength of the magnetic pinning [domain

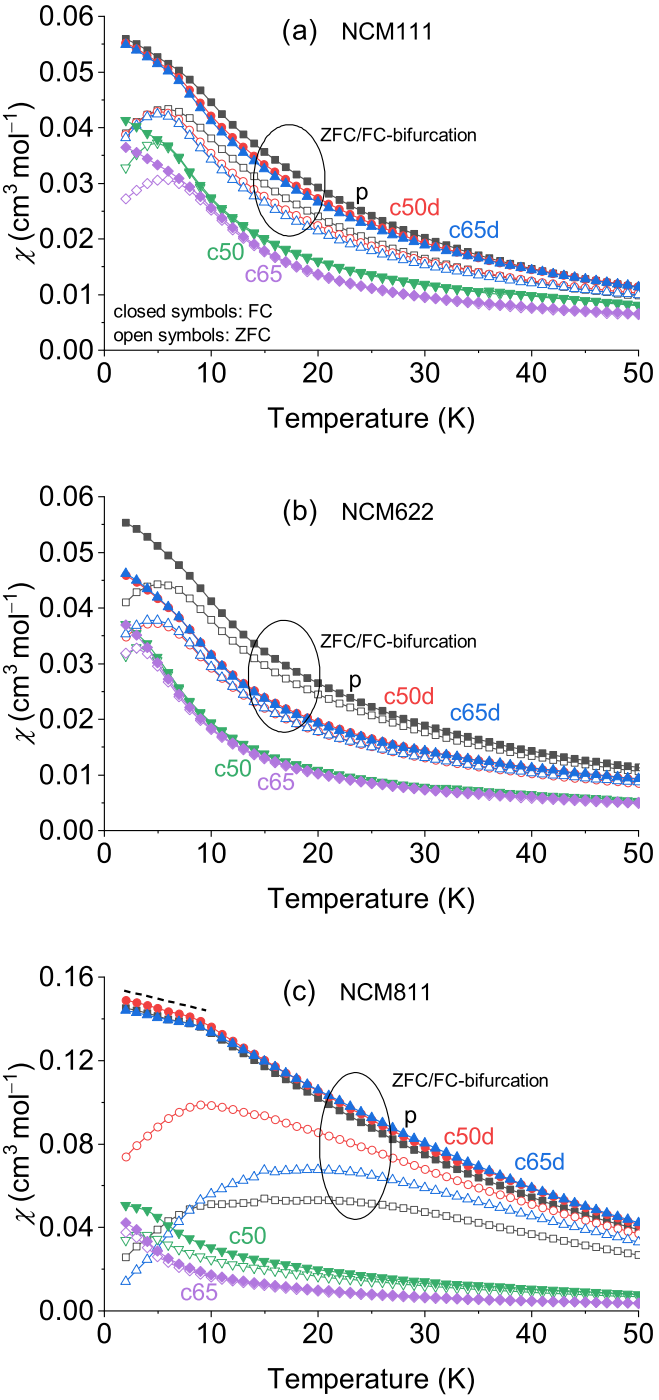

FIG. 4. Low-temperature section (below 50 K) of the ZFC/FC susceptibility curves for (a) NCM111, (b) NCM622, and (c) NCM811 at various states of charge. The areas $\Delta A_{FC/ZFC}$ enclosed between the ZFC and FC susceptibility curves for temperatures >10 K and the temperatures of local maxima of the FC susceptibility curves T_{FC}^{max} are plotted in Fig. 5.

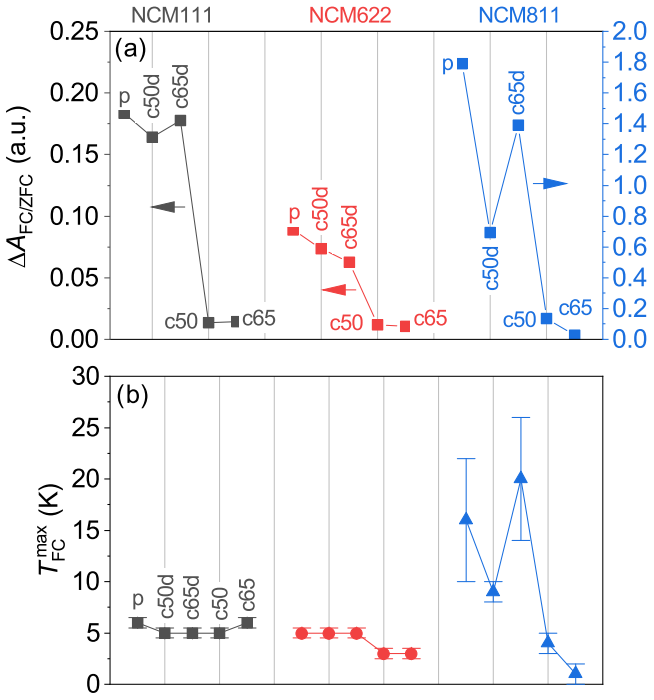

FIG. 5. Area $\Delta A_{FC/ZFC}$ enclosed between the ZFC and FC susceptibility curves for temperatures >10 K and the temperatures of local maxima of the FC susceptibility curves T_{FC}^{max} as determined from the plots shown in Fig. 4.

wall movement in the case of ferro-/ferrimagnetic order or spin freezing in the case of a spin-glass (SG) or a cluster-glass (CG)] that can be overcome when this temperature is passed during the heating process of the measurement. It should be noted that these T_{FC}^{max} values are specific for the applied DC magnetic field of 500 Oe. For NCM811 and NCM622, T_{FC}^{max} values are a little bit higher for the discharged than for the charged states and for NCM811 the absolute values of the discharged states p, c50d, and c65d are larger than those of NCM622 and NCM111. Another detail should also be noted: The FC curves of discharged NCM811 (p, c50d, c65d) below T_{FC}^{max} have a more horizontal progression [highlighted by the dashed line in Fig. 4(a)] than the FC curves of discharged NCM622 and NCM111, in agreement with the results from AC susceptibility presented below that reveal stronger spin-glass-like characteristics for the magnetic transition below about 10 K for NCM811 material compared to NCM622 and NCM111.

2. Fieldscans

Figure 6 shows the magnetization vs magnetic field scans at 2 K for all compositions and states of charge (those measured at 300 K are shown in Fig. S9 within the SM [38]). At 300 K, magnetic exchange coupling and/or local anisotropies play a negligible role and the corresponding field scans exhibit a linear progression. Therefore, the magnetization values M_{70kOe}^{300K} measured at 70 kOe are proportional to the samples' susceptibility at 300 K to good approximation and strongly depend on the samples' effective moments μ_{eff} that are discussed in detail below in Sec. III D 3. M_{70kOe}^{300K} for the pristine state (p) is decreasing in the order NCM111-p, NCM622-p, NCM811-p, as plotted in Fig. 7(a). Delithiation strongly decreases M_{70kOe}^{300K}, but this decrease is not strictly proportional to the degree of delithiation x but saturates quickly for $x > 0.5$, proposedly owing to the relaxation processes occurring in the hours after highly charging to $x = 0.65$, as outlined in

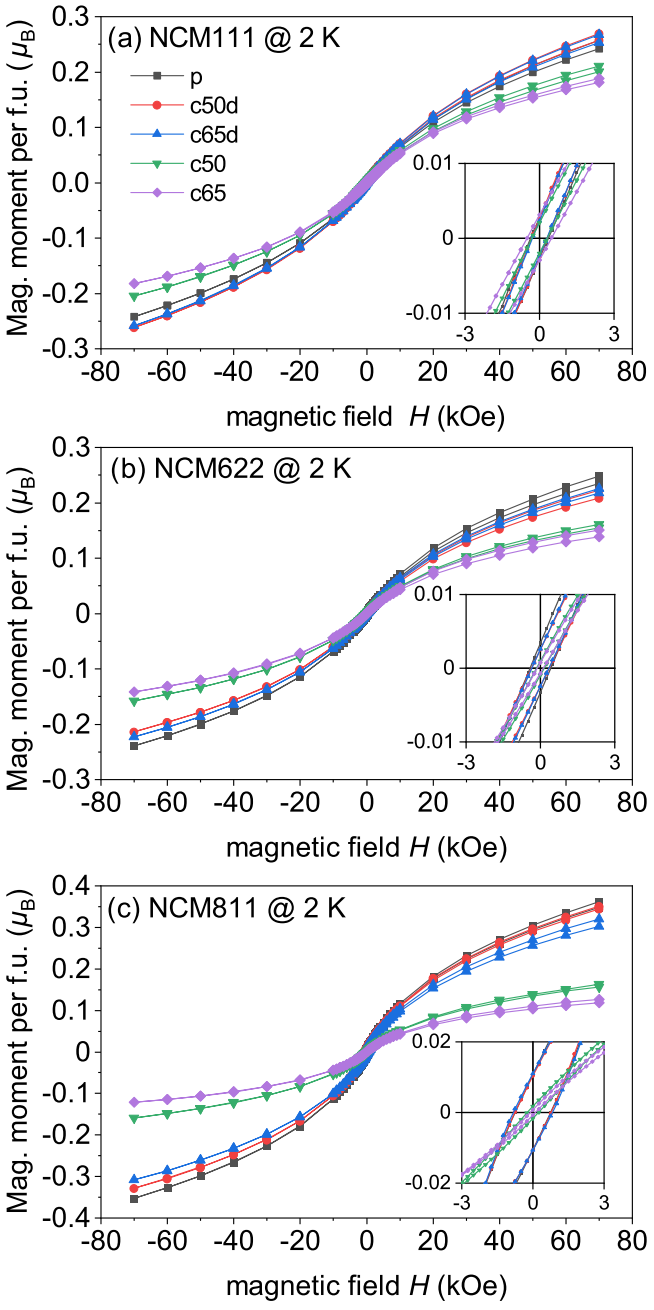

FIG. 6. Magnetic moment vs magnetic field plots measured at 2 K for (a) NCM111, (b) NCM622, and (c) NCM811 in various states of charge. The insets display enlarged sections to more clearly illustrate the magnetic coercivity. The field scans measured at 300 K are presented in Fig. S9 within the SM [38]. All extracted parameters from the field scans are plotted in Fig. 7.

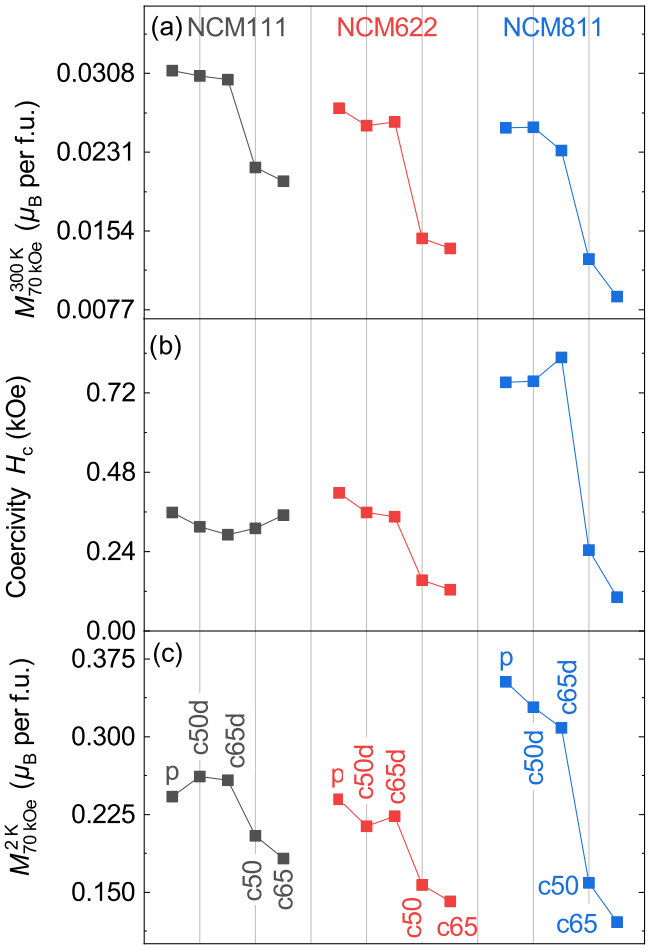

FIG. 7. Parameters extracted from the magnetic moment vs magnetic field scans. (a) Magnetic moment per f.u. measured at 300 K at a field of 70 kOe M^{300K}_{70kOe}. (b) Magnetic coercivity field H_c at 2 K, and (c) magnetic moment per f.u. measured at 2 K at a field of 70 kOe M^{2K}_{70kOe}.

Sec. III C above. The fact that the values of the discharged states (c50d and c65d) are still below that of the pristine state indicate the presence of irreversible processes occurring during initial charging.

From the field scans at 2 K that were measured after cooling the sample down in a field of 70 kOe (Fig. 6), the maximal measured magnetization M^{2K}_{70kOe} at field of 70 kOe and the coercivity field H_c have been determined and are plotted in Figs. 7(b) and 7(c), respectively. The fact that the magnetization curves at 2 K have not yet saturated at 70 kOe demonstrates that the magnetic spins cannot freely align along the external field and that local anisotropy and/or antiferromagnetic or Dzaloshinskii–Moriya [52] (canted antiferromagnetic) exchange coupling and/or some type of spin freezing hinders saturation even up to 70 kOe. The M^{2K}_{70kOe} values show a similar trend as found for M^{300K}_{70kOe} (and also μ_{eff}) at first sight. This is because only those compositions and states of charge that lead to large magnetic moments of the individual TM ions can finally also contribute with large ordered magnetic moments. However, for the low-temperature M^{2K}_{70kOe} values the type of magnetic ordering plays a crucial role, of course. It is remarkable that for discharged NCM811 (p, c50d, and c65d), the M^{2K}_{70kOe} values are significantly higher than those of the discharged states (p, c50d, and c65d) of NCM111 and NCM622, even though for the M^{300K}_{70kOe} values (and also for μ_{eff} values) the opposite holds. The reason is that a FM mean-field coupling, parameterized by the Weiss constant θ_{CW}, has been found for NCM811-p, c50d and c65d, whereas for all other samples and charging states an AFM mean-field coupling has been determined ($\theta_{CW} < 0$), as outlined below

in more detail. The coercivity fields at 2 K are largest for the NMC811-p, c50d, and c65d discharged states (around 750 Oe) and decrease considerably for the NMC811-c50, -c65 charged states (around 200 Oe). Less pronounced, this trend can also be observed for NCM622, where the coercivity decreases from around 350 Oe for the NCM622-p, c50d, c65d discharged states to around 180 Oe for the NMC622-c50, -c65 charged states. For NCM111, the coercivity field remains approximately at around 300 Oe for all states. A coercivity field of 11(1) Oe has been reported for NCM111 and a value of 1316(2) Oe for $LiNi_{0.5}Mn_{0.5}O_2$ in literature, for instance [11]. NCM811 (p, c50d, c65d) exhibits a significantly higher coercivity field at 2 K than NCM622 and NCM111 (p, c50d, c65d). It remains unclear whether the increased coercivity field is physically related to the stronger spin-glass-like characteristics of the low-temperature magnetic transition that is clearly indicated to be realized for NCM811 (p, c50d, c65d) by a more horizontal FC susceptibility curve and a more pronounced relative frequency shift of the χ' AC susceptibility signal.

3. *Effective magnetic moment and TM oxidation states*

The inverse susceptibility χ^{-1} vs temperature plots from 100 to 300 K that have been measured at an increased field of 5 kOe (in order to saturate pre-ordered magnetic clusters and to minimize their temperature-dependent contributions) are presented in Figs. S10–S12 within the SM [38] together with Curie-Weiss fits according to Eq. (1) from 100 to 300 K for all compositions and states of charge. The effective magnetic moments μ_{eff} were calculated from the Curie constant C_c and are plotted in Fig. 8(a). Similarly to the $M^{300\text{K}}_{70\text{kOe}}$ values, μ_{eff} decreases considerably from NCM111-p to NCM622-p and to NCM811-p. For a specific composition, μ_{eff} strongly decreases with increasing amount of delithiation x. A saturation behavior for $x > 0.5$ is more pronounced for NCM111 than for NMC811 material, proposedly owing to the relaxation processes occurring in the hours after highly charging to $x = 0.65$ as outlined in Sec. III C above. An irreversibility, in the sense that the μ_{eff} values do not return back to their initial value of the corresponding pristine material cannot be inferred from these curves. The Weiss constants θ_{CW} for NCM111 and NCM622 are all negative, pointing to an overall AFM mean-field coupling [see Fig. 8(b) that also presents values from other publications for comparison]. It is hard to claim a trend in dependence on the state of charge here. Interestingly, all discharged states of NCM811 (p, c50d, and c65d) exhibit positive θ_{CW} values indicating a dominant FM mean field coupling, but the charged states of NCM811 (c50, c65) exhibit again AFM mean field coupling with negative θ_{CW} values. As outlined above, the determined θ_{CW} explain well the evolution of the $M^{2\text{K}}_{70\text{kOe}}$ values for the different samples. In contrast to the findings of this paper, Wikberg *et al.* [53,54] have found a similar effective magnetic moment of 2.07 μ_B, but a negative $\theta_{\text{CW}} = -25$ K value for NCM811 by a DC magnetometry measurement at 100 Oe (to the best knowledge of the authors, more published θ_{CW} values for NCM811 are not available in literature up to date). It should be noted that for the pure Ni containing compositions $Li_{0.996}Ni_{1.004}O_2$ [19], $Li_{\sim 0.99}Ni_{\sim 1.01}O_2$ [26], and $Li_{0.98}Ni_{1.02}O_2$ [25] also positive

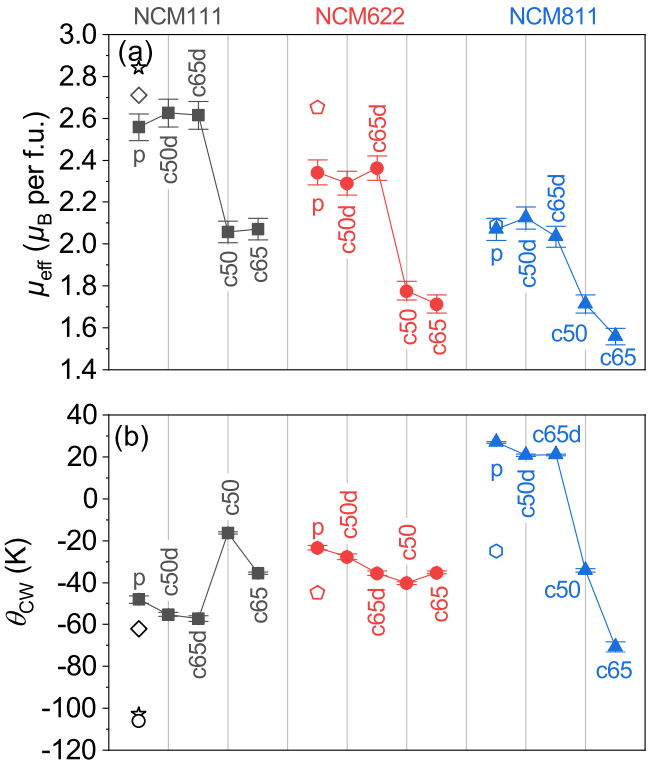

FIG. 8. (a) Effective magnetic moments μ_{eff} and (b) Weiss constants θ_{CW}, extracted from the Curie-Weiss fit to the susceptibility vs temperature curve from 100 to 300 K (see Figs. S10–S12 within the SM [38]). Diamonds, Chernova *et al.* [11]; stars, Mauger *et al.* [14]; circles, Xiao *et al.* [82]; pentagons, Ye *et al.* [40]; hexagons, Wikberg *et al.* [53,54].

Weiss constants of +26, +29.5, and +18 K, respectively, have been determined. Therefore, a transition from positive to negative θ_{CW} values is definitely expected to occur between the compositions $LiNiO_2$ and $LiNi_{0.6}Co_{0.2}Mn_{0.2}O_2$. A reason for the discrepancy concerning the determined Weiss constant for NCM811-p might be the fact that in Refs. [53,54] a cation mixing of 3.9% had been determined that is significantly above that value that has been determined in this work for NCM811-p [see Fig. 8(a)]. The magnetic properties of this class of materials are strongly affected by the structural details, for instance by the Ni/Co/Mn cation disordering and even more decisively by the Li/Ni site disordering, both depending on the specific route of synthesis. Therefore, samples with the same nominal composition might still be different concerning these structural details that decisively determine the magnetic properties. As illustrated in Fig. S8d within the SM [38], the detailed progression of the inverse susceptibility χ^{-1} vs temperature in the range 100–300 K for NCM811-p depends on whether the applied field was 0.5 kOe (as used for the ZFC/FC susceptibility measurements with high sensitivity for irreversibilities in this paper) or 5 kOe (as used for the determination of the effective magnetic moments by Curie-Weiss fits from 100 to 300 K in this paper) owing to the magnetic cluster formation that also occurs in this temperature range [10]. However, a Curie-Weiss fit to χ^{-1} obtained at only 0.5 kOe from 250 to 300 K returns very similar values for $\theta_{\text{CW}} = +32(1)$ K and $\mu_{\text{eff}} = 2.07(5)\,\mu_B$ as

obtained for the measured at 5 kOe [$\theta_{CW} = +27(1)$ K and $\mu_{eff} = 2.07(5)\,\mu_B$], thereby excluding a strong field effect that could explain the discrepancy with the values published in Refs. [53,54].

In this paper, the spin-only magnetic moment that results from the total spin S according to $\mu_{eff} = g_S\sqrt{S(S+1)}\mu_B$, with the electron g factor $g_S \approx 2$, will be considered as an approximation and all contributions from angular orbital momentum will be ignored. For ideal octahedral crystal field, the orbital momentum would indeed be quenched for Ni^{2+}, Ni^{3+}, Ni^{4+}, Co^{3+}, and Mn^{4+} that are most relevant for the investigated NCM systems. For Ni, Co, and Mn, Table S5 within the SM [38] lists, for all considered redox states +2, +3, and +4, the number n of d electrons for the electronic configurations $[Ar]3d^n$, the corresponding occupation of the threefold degenerated t_g states (at lower energy) and the twofold degenerated e_g states (at higher energy) for a hypothetically ideal octahedral crystal field in the low-spin (LS) state, the corresponding total spin angular momentum quantum number S, and the effective magnetic spin-only moment μ_{LS}^{SO}. Most importantly, for this paper, Ni^{2+}, Ni^{3+}, and Ni^{4+} are assumed to be present as $S = 1$ (2.83 μ_B), $S = 1/2$ (1.73 μ_B), and $S = 0$ (diamagnetic), respectively, Mn^{4+} and Mn^{3+} as $S = 3/2$ (3.87 μ_B) and $S = 1$ (2.83 μ_B), and Co^{3+} as $S = 0$ (diamagnetic). It should be mentioned that a diamagnetic Ni^{4+} ion species has formally been introduced for this paper, but that recent publications suggest that charging of $Li_{1-x}NiO_2$ and other related materials containing Ni^{3+} rather leads to the formation of a covalent Ni^{3+} species together with a partial oxidation of oxygen instead [45,55]. However, results from magnetic susceptibility measurements [21] and NMR spectroscopy investigations [9] on $Li_{1-x}NiO_2$ clearly reveal that charging results in a reduction of the effective magnetic moment. The remaining unpaired electron that would formally be present for Ni^{3+} (see Table S5 within the SM [38]) can illustratively be thought to be paired with an unpaired electron from the partially oxidized oxygen in the covalent bond, leading to an overall reduced magnetic moment again. For simplicity, the oxidized species of Ni^{3+} will be labeled as Ni^{4+} in this paper reflecting also a reduced magnetic moment compared to Ni^{3+}.

A numerical approach has been applied to connect the redox states of the contributing Ni, Co, and Mn ions with the total measured effective magnetic moment μ_{eff}. Therefore, an average redox state ranging from +2 to +4 was ascribed to each of the TM Ni, Co, and Mn, individually. This average redox number represents a bimodal distribution of the discrete oxidation states +2, +3, and +4 for each TM. For example, an average redox state of +2.75, ascribed to a certain TM, would be represented by 25% TM^{+2} and 75% TM^{+3}, and a redox state of +3.5 would be represented by 50% TM^{+3} and 50% TM^{+4}, but there will be no disproportion into a contribution from +2 and +4 at the same time for a TM within this framework. With the constraint of charge neutrality (Li and O are assumed to be present as Li^{+1} and O^{-2}), a solid line laying within a colored area in Fig. 9 represents the average value of the measured effective magnetic moment μ_{eff} (solid lines) and the colored area around the solid line represents the errors of these experimental values [see Fig. 8(a)]. Each point in the 2D diagram can be assigned to a combination of Ni (x axis), Mn (y axis), and Co (number connected to the dashed lines) redox states.

Comparison of pristine states. Figure 9(a) compares the pristine states of NCM111-p, NCM622-p, and NCM811-p with each other. For NCM111-p, an average effective magnetic moment $\mu_{eff}^{avg} = 2.56\,\mu_B$ has been measured. From the XAS analysis (see Sec. III D 4), it seems justified to set the Co redox state to +3 for all samples and states of charge as a first approximation that is also applied throughout the literature for NCM materials. A Co redox state of +3 means that only those combinations of redox states laying on the dashed line going through point A in Fig. 9(a), are selectable. Point A exemplarily represents the combination $Ni^{+2.3}$, Co^{+3}, and $Mn^{+3.7}$ that would in combination create the measured μ_{eff}^{avg} value. For NCM622-p an average effective magnetic moment μ_{eff}^{avg} of 2.34 μ_B has been measured. Fixing the Co oxidation state to +3 again, this value could be reproduced by the combination $Ni^{+2.7}$, Co^{+3}, and $Mn^{+3.8}$ (point B), i.e., the Ni oxidation would have considerably be increased from +2.3 to +2.7, and that of Mn slightly from +3.7 to +3.8 compared to NCM111-p. For NCM811-p, an average effective magnetic moment $\mu_{eff}^{avg} = 2.07\,\mu_B$ has been measured. Fixing the Co oxidation state again to +3, this value could be reproduced by the combination $Ni^{+2.9}$, Co^{+3}, and $Mn^{+3.9}$ (point C), i.e., the Ni oxidation would further be increased slightly from +2.7 to +2.9, and that of Mn from +3.8 to +3.9 compared to NCM622-p.

Generally, the reduction of Ni from +3 to +2 is connected with an increase of μ_{eff} from 1.73 to 2.83 μ_B, and the oxidation of Mn from +3 to +4 (to compensate the Ni reduction) is also connected with an increase of μ_{eff} from 2.83 to 3.87 μ_B, both leading to larger overall μ_B values. The ratio of Ni to Mn (and Co) strongly increases in the order NCM111, NCM622, and NCM811. As a consequence, for NCM811 a much smaller amount of Ni can be reduced by a simultaneous oxidation of the same amount of Mn than for NCM111 and a correspondingly higher amount of Ni with a higher oxidation state (closer to +3) with a reduced measured μ_{eff} value results for NCM811 compared to NCM111. Overall, the trends of a comparably strong increase of the Ni redox state from +2.3 to +2.7, and further to +2.9 and the comparably weak increase of the Mn redox state from +3.7 to +3.8, and further to +3.9 in the order NCM111-p, NCM622-p, and NCM811-p, are also reflected by the shifts of the Ni and the Mn K-edge positions, respectively (see XAS analysis in Sec. III D 4). If only Mn^{4+} would be assumed to be present while the same amount of Ni would have been reduced from Ni^{3+} to Ni^{2+} for charge compensation, and if the Co redox state would be fixed to Co^{3+} (as done in Refs. [14,56], for instance), the average Ni redox state would increase from +2, to +2.66, and to +2.875 [points A″, B″, and C″ in Fig. 9(a)] with the effective magnetic moments decreasing from 2.77, to 2.34, and to 2.01 μ_B, in the order NCM111-p, NCM622-p, and NCM811-p, respectively. Most pronounced for NCM111 with equal amounts of Mn and Ni, the predicted effective magnetic moment of 2.77 μ_B for all Mn being present as Mn^{4+} and all Co as Co^{3+} is not in agreement with the much smaller experimentally observed average effective magnetic moment of only about 2.56 μ_B in this paper. Within the framework of the applied assignments of magnetic moments to the TMs'

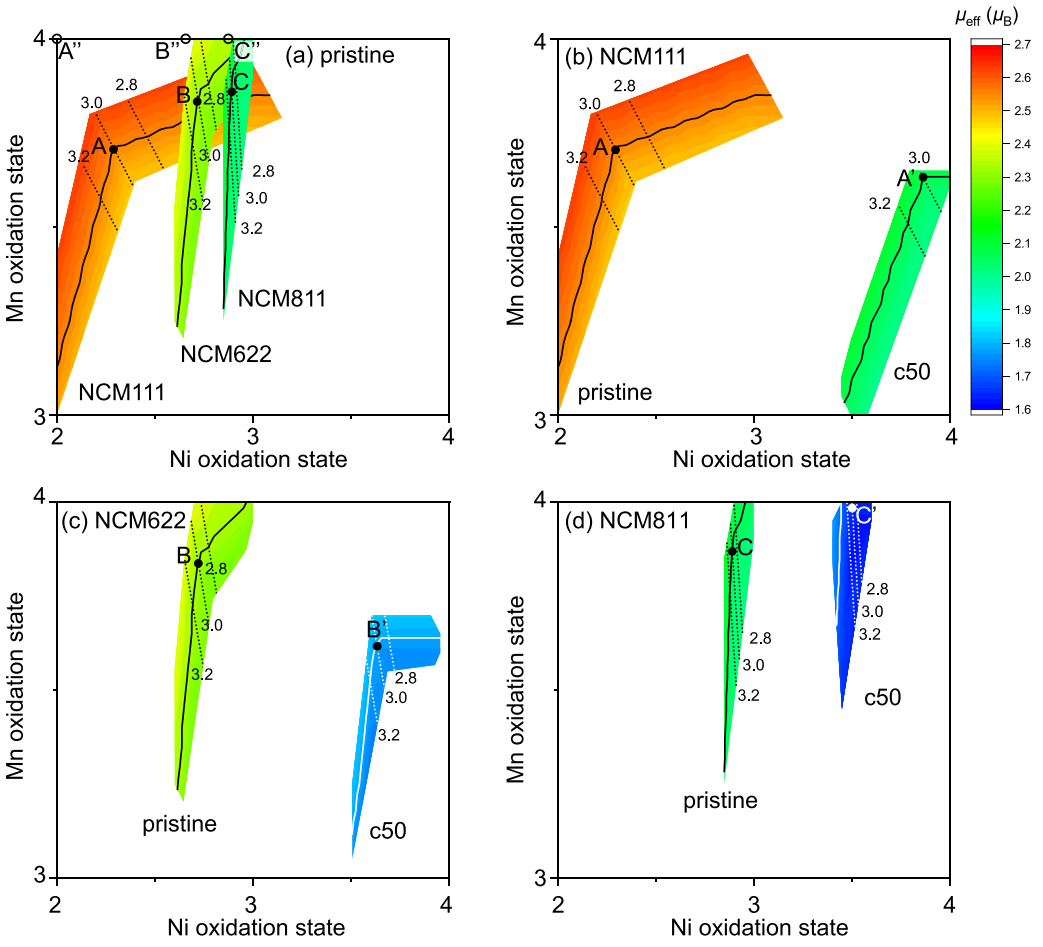

FIG. 9. Relation of Ni, Co, and Mn redox states and effective magnetic moment μ_{eff}. Comparison of (a) pristine states NCM111-p, NCM622-p and NCM811-p with each other; (b) NCM111-p with NCM111-c50; (c) NCM622-p with NCM622-c50; (d) NCM811-p with NCM811-c50. The solid lines represent the average values of the measured μ_{eff} and the coloured areas span the errors of μ_{eff}. The dotted lines represent the Co redox state number. The meaning of the characters are described in the main text.

oxidation states (Table S5 within the SM [38]), a Mn oxidation state slightly below +4 depending on the elemental composition of the NCM material is necessary to explain the experimental observations here.

Comparison of pristine state with charged state. Figure 9(b) shows how the effective magnetic moment depends on the redox states of Ni, Co, and Mn for the NCM111 material in the pristine state and delithiated to $x = 0.5$ (c50). For a chosen Co oxidation state of +3, the average effective magnetic moment $\mu_{\text{eff}}^{\text{avg}} = 2.56\,\mu_B$ for the pristine NCM111-p is represented by point A again ($Ni^{+2.3}$, Co^{+3}, and $Mn^{+3.7}$). For the delithiated NCM111-c50, an average effective magnetic moment $\mu_{\text{eff}}^{\text{avg}} = 2.06\,\mu_B$ has been measured. Under the assumption that the Co oxidation state remains +3 (point A′), that moment could be realized for the oxidation states $Ni^{+3.9}$, Co^{+3}, and $Mn^{+3.6}$, i.e., essentially by a strong oxidation of Ni from +2.3 to 3.9 whereas Mn is supposed to be slightly reduced.

Figure 9(c) shows the corresponding correlations for the NCM622 material. For a chosen Co oxidation state of +3, the average effective magnetic moment $\mu_{\text{eff}}^{\text{avg}} = 2.34\,\mu_B$ for the pristine NCM622-p is represented by point B again ($Ni^{+2.7}$, Co^{+3}, and $Mn^{+3.8}$). For the delithiated NCM622-c50, an average effective magnetic moment $\mu_{\text{eff}}^{\text{avg}} = 1.78\,\mu_B$ has been measured. Under the assumption that the Co oxidation state remains +3 (point B′), that moment could be realized for the oxidation states $Ni^{+3.6}$, Co^{+3}, and $Mn^{+3.6}$, i.e., essentially by a strong oxidation of Ni from +2.7 to 3.6 whereas Mn is supposed to be slightly reduced.

Figure 9(d) shows the corresponding correlations for NCM811. For a chosen Co oxidation state of +3, the average effective magnetic moment $\mu_{\text{eff}}^{\text{avg}} = 2.07\,\mu_B$ for the pristine NCM811-p is represented by point C again ($Ni^{+2.9}$, Co^{+3}, and $Mn^{+3.9}$). For the delithiated NCM811-c50, an average effective magnetic moment $\mu_{\text{eff}}^{\text{avg}} = 1.71\,\mu_B$ has been measured. Under the assumption that the Co oxidation state remains +3 (point C′), that moment could be obtained for the oxidation states $Ni^{+3.45}$, Co^{+3}, and $Mn^{+3.99}$, i.e., essentially by a strong oxidation of Ni from +2.9 to 3.45 and a further slight oxidation of Mn from +3.9 to 3.99. The proposed small changes of the Mn redox state within the framework of the applied magnetic model should be considered critically, since they cannot unambiguously be confirmed by the results from the XAS measurements as outlined in the following section. As

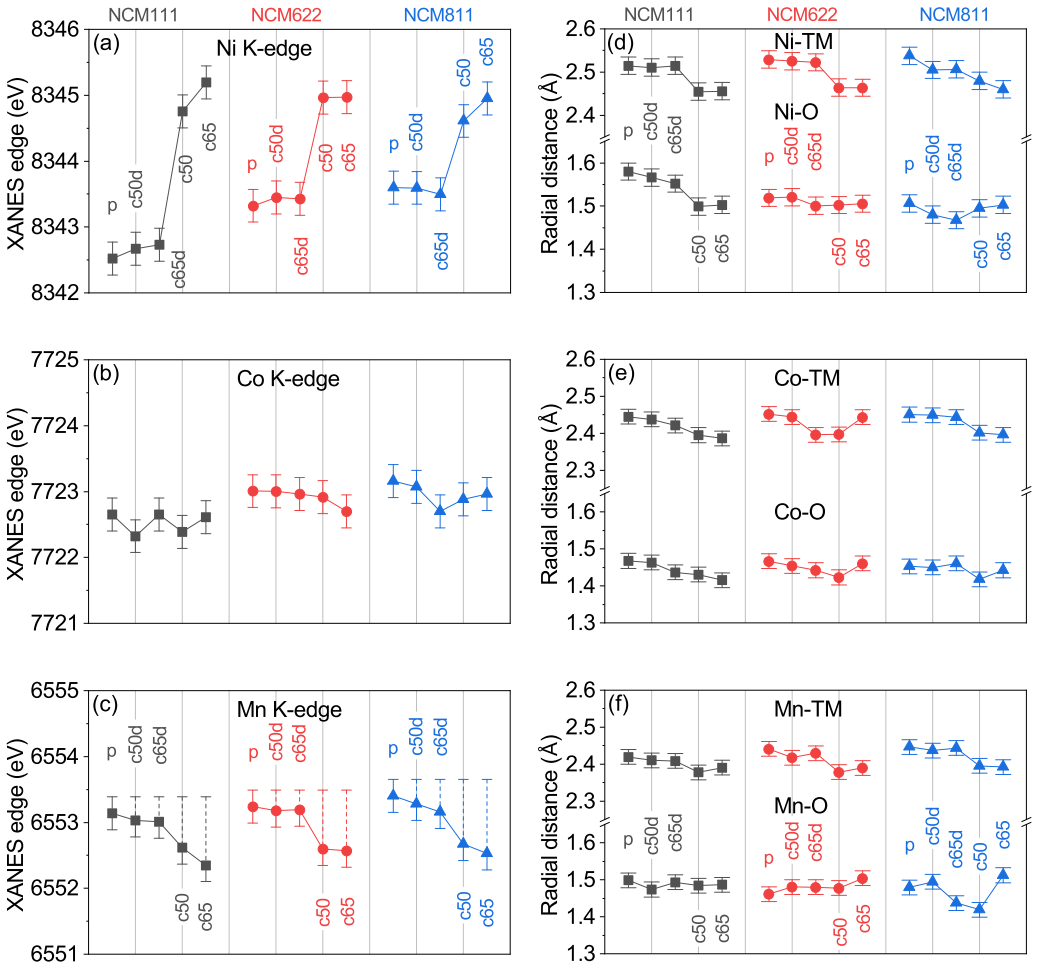

FIG. 10. Extracted parameters from XAS measurements obtained for NCM111, NCM622, and NCM811 at all states of charge. The K-edge positions where determined as the energy where the absorption reaches 50% of the edge height from the (a) Ni, (b) Co, and (c) Mn K-edge absorption spectra (see also Figs. S13–S15 within the SM [38]). Radial distances (d) Ni-TM and Ni-O, (e) Co-TM and Co-O, and (f) Mn-TM and Mn-O, determined from the Fourier transformed (FT) of the k^3-weighted EXAFS oscillations (see also Figs. S17–S19 within the SM [38]). The obtained radial distances of the FT are not phase-shift corrected.

can be nicely inferred from Fig. 9, there are no other trivial combinations of TM oxidation states to explain the measured effective magnetic moments more reasonably. For instance, if a constant Mn-oxidation state (close to +4) would be assumed to be present for all pristine states, this would necessarily affect the Co (and also the Ni) redox states in a way that would not be in agreement with the results from XAS either, where Co is supposed not to change noticeably. All deviations from what is covered by the applied simplified magnetic model—such as contributions to the effective magnetic moment due to partially oxidized oxygen species, contributions from orbital angular momentum, effects from Jahn-Teller distortions, contributions from high-spin species, or also inhomogeneous delithiation as indicated for certain compositions by NMR spectroscopy (see Sec. III D 5 below)—might accidently cause the aforementioned "predictions" that the Mn redox state would slightly change. However, implementation of all these further contributions to the magnetic moment into a magnetic model is very challenging and beyond the scope of this paper. Still, the main conclusion that Ni contributes by far most to the charge compensation are confirmed by these magnetic susceptibility measurements and other conclusions drawn in this paper about the magnetic transitions and so forth are not affected significantly by these details.

4. X-ray absorption spectroscopy

Figures S13–S15 within the SM [38] present the x-ray absorption spectra of the Ni, Co, and Mn K-edge, respectively, that have been measured for all compositions NCM111, NCM622, and NCM811 at all states of charge (p, c50, c65, c50d, c65d). From these spectra, the K-edge positions were determined as the energy where the absorption reaches 50% of the maximum edge height and are plotted in Figs. 10(a)–10(c). Most importantly, the Ni K-edge positions that indirectly reflect the Ni ions' redox states, qualitatively exhibit the same dependence on the composition and on the state of charge as the effective magnetic moments [Fig. 8(a)]. For instance, for the pristine states the Ni redox state has been determined to +2.3, +2.7, and +2.9 for NCM111, NCM622, and NCM811, respectively, from the effective magnetic moments. These Ni redox states are in agreement with the Ni K-edge positions

for these pristine states when compared directly with the reference compounds Ni(II)O and LiNi(III)O_2 (see Fig. S16 within the SM [38]).

Taking the uncertainties (error bars) of the K-edge positions into account, the Co redox state can reasonably be assumed to be independent of composition and state of charge [Fig. 10(b)]. This justifies to some extent to keep the Co oxidation state constant at +3 as done in Sec. III D 3, even though it is hard to determine the absolute oxidation state of Co by a comparison with the reference compounds Co(II)O and LiCo(III)O_2 (see Fig. S14 within the SM [38]) that are nonisostructural to NCM and exhibit a different shape of the absorption edge in general.

In contrast to the Ni K-edge, that approximately retains its shape and only shifts in energy during charging, the Mn K-edge more drastically changes its shape (see Fig. S15 within the SM [38]). This might be caused by the change of lattice parameters and TM-O slab thicknesses during charing (see Fig. 3) that also affect details of the Mn's local oxygen coordination and in turn alter the Mn K-edge shape (see also the discussion of the EXAFS results below). Therefore, changes of the local Mn oxygen coordination might be responsible for the slight shifts of the Mn K-edge positions to lower energies at 50% absorbance that can be observed for the charged states c50 and c65 of all compositions. Still, a partial reduction of Mn cannot be ruled out to also contribute to the energy shift based on the K-edge analysis. To make this circumstance clear, corresponding error bars (dashed lines) towards higher energies have been inserted for the determined Mn K-edge positions in Fig. 10(c). The Mn K-edge of the pristine NCM materials resembles most that of the reference compound Mn(IV)O_2 and, therefore, Mn can reasonably be assumed to be present close to Mn^{4+}. The average values of the Mn's K-edge position suggest a slight increase of the Mn's oxidation state for the pristine states (with very similar structure for all compositions) in the order NCM111-p, NCM622-p, and NCM811-p. A slight increase of the oxidation state would be in line with what has been suggested by the determination of the Mn's oxidation state of the pristine states from the effective magnetic moment within the applied magnetic model (see above).

Figures S17–S19 within the SM [38] present the Fourier transformed (FT) of the k^3-weighted EXAFS oscillations calculated for the Ni, Co, and Mn K-edge, respectively, for all compositions NCM111, NCM622, and NCM811 and for all states of charge (p, c50, c65, c50d, c65d). From these spectra, the radial distances TM-O and TM-TM have been determined and are plotted in Figs. 10(d)–10(f). In general, oxidation of the TMs in the NCM materials cause the unit cell volume V to shrink slightly (the increase of the c lattice parameter is over compensated by the decreasing a and b lattice parameters; see also Sec. III C) before degradation processes set in for very high states of charge [4,46]. As a consequence, the radial distances TM-O and TM-TM reproduce the trend observed for the redox state of the TMs by exhibiting smaller values when the TMs are oxidized, for example. It should be noted that despite the fact that Ni is mainly contributing to the charge compensation during charging/discharging also the Co-O/Co-TM, and Mn-O/Mn-TM distances are affected in a quite similar way. This is because local changes of the Ni-O coordination affect the crystal lattice on a long-range scale, thereby also modifying the local oxygen coordinations of the Co and Mn ions.

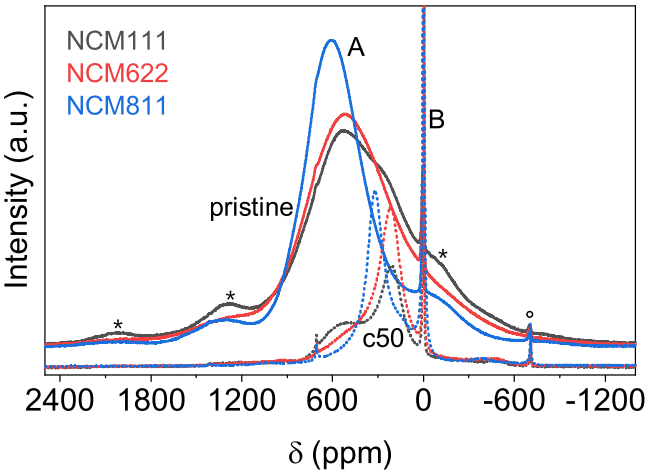

FIG. 11. ^{7}Li solid-state NMR spectra of NCM111, NCM622, and NCM811 in pristine (p) state (solid lines) and charged to $x = 0.5$ (c50; dashed lines). Different NMR signals are labeled with A and B corresponding to the Li signals of the NCM phase and the residual Li salts, respectively. Asterisks and open cycles denote the spinning sidebands.

5. Nuclear magnetic resonance

^{7}Li solid-state NMR experiments were performed on NCM111, NCM622, and NCM811 in the pristine (p) state and charged to $x = 0.5$ (c50). For such NCM materials, including paramagnetic neighbors, the ^{7}Li NMR shifts are dominated by the Fermi contact interaction, induced by the delocalization of unpaired electron spin density from Ni/Mn d orbitals to the Li nucleus via the bridging oxygen atoms [57,58]. Based on earlier experimental research on $LiNi_{0.02}Mn_{0.02}Co_{0.96}O_2$, 90° and 180° Ni-O-Li interactions can induce NMR shifts of −15 and 110 ppm, and 90° and 180° Mn-O-Li interactions induce shifts of 258 and −53 ppm, respectively [59]. Figure 11 shows two main NMR signals for the pristine samples, which correspond to Li in NCM materials (A) and to Li in diamagnetic salts like Li_2CO_3 and LiOH (B). Spinning sidebands from signals A and B are marked with asterisks and open circles. Signal A, representing the different Li environments in the NCM materials, is very broad, covering a range of several hundred ppm. This is caused by the many different environments that are present around Li in these layered structures. While the nearest neighbors around Li on a regular 3a Wyckoff site are six oxygen ions forming an octahedron, behind these oxygen ions there are six Li next-nearest neighbors (within the Li layer) and 12 TM neighbors (in the TM layer) connected via 90° and 180° Li-O-TM bonds. As mentioned above, the TM neighbors are inducing the large shifts observed for these compounds. For a random arrangement of Ni/Mn/Co in the TM layers, there are many different environments around Li that differ in numbers of Ni/Mn/Co neighbors but also their arrangement around Li. Superposition of the many different contributions of these different environments results in the broad lines. Further broadening of this

line can be caused by Jahn-Teller distortions leading to variations in the Ni-O bond lengths [60]. Another reason for the broad lines can be the presence of Li/Ni mixing between the layers, in agreement with the results from Rietveld analysis (Fig. 3).

Genreith-Schriever *et al*. proved that Li in the TM layers can induce NMR signals between 420 and −69 ppm and the exact values are determined by the relative position between Li in the TM layers and Ni in the Li layers [61]. The Ni in Li layers would generate different environments for the neighboring Li in the Li layers, and the corresponding signals appear on the left side of peak A. While the diversity of these environments is maximum for NCM111 with same amounts of Co/Ni/Mn, for the Ni-richer systems environments with more Ni occur with higher probability. This can be seen in the ^{7}Li NMR spectra, where the broadest spectrum is observed for NCM111. When going to the Ni-richer sytems (NCM622 and NCM811), the overall width of peak A is getting smaller and its maximum is shifting to the left, to higher (more positive) NMR shifts. One reason for this is the presence of less diamagnetic Co^{3+}, where the NMR shift contribution is negligible in comparison to those of Mn/Ni. Regarding the spectra of the three charged electrodes, signal A shifts to lower ppm positions for all three samples owing to the partial loss of Ni^{3+}-O-Li interactions (110 ppm) when some of the Ni^{3+} ions are oxidized to Ni^{4+} on Li removal as also revealed by the XAS analysis (Sec. III D 4) and the determination of TM redox states from the effective magnetic moments (Sec. III D 3). Interestingly, for the charged NCM111-c50 sample, two signals at 550 ppm and 220 ppm are observed, in agreement with results from Yoon *et al*. [62]. The former one corresponds to Li in Li-richer domains [62–64] where Ni^{3+} ions are still dominating, thus hinting at inhomogeneous delithiation of these materials, e.g., by two-phase reactions or slow delithiation kinetics, as it was recently also observed by *operando* light microscopy [65]. Such an inhomogeneous delithiation might also contribute to the anisotropic strain described above. For the NCM622-c5 and NCM811-c5 samples, the intensity of the left peak is strongly decreased, again in agreement with earlier results [63], thus hinting at a more homogeneous delithiation.

6. AC magnetometry

The real χ' and imaginary χ'' part of AC susceptibility have been measured from 50 to 2 K in zero DC magnetic field for all compositions and states of charge (for NCM111 only in the pristine state). Figure 12 compares the AC susceptibility data measured for the pristine materials NCM111-p, NCM622-p, and NCM811-p. Firstly, the absolute values of χ' and χ'' are considerably larger for NCM811-p than for NCM111-p and NCM622-p. All compositions have in common that χ' first increases monotonically from 50 K down to the maximum at $T^{L}_{\chi'} \approx 8$ K, before it decreases down to 2 K [Fig. 12(a)]. For NCM811-p, this maximum exhibits a relative frequency shift $\Delta T^{H}_{\chi'}/[T^{H}_{\chi'}\Delta(\lg\omega)]$ of about ∼2.2% [Fig. 12(c)] that lies in between the typical value of ∼1% for spin glass (SG) and the typical value of ∼5% for cluster glass (CG) [66]. In contrast, for NCM622-p and NCM111-p, no relative frequency shift of the maximum of χ' can

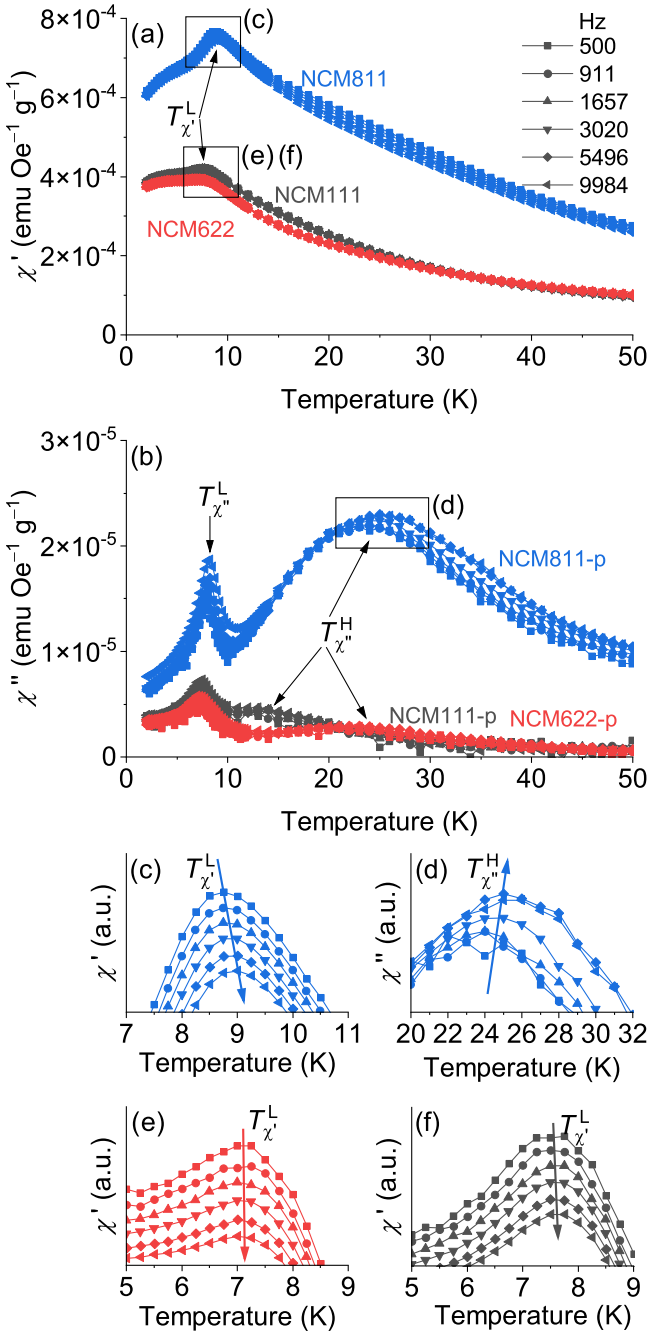

FIG. 12. Measured AC susceptibility (a) χ' and (b) χ'' vs temperature plots for pristine NCM111, NCM622, and NCM811 sample material at zero DC magnetic field. (c)–(f) show enlarged sections of what is presented in (a) and (b) with relative frequency shifts (indicated by arrows) of the transitions. Error bars have been omitted for clarity.

be observed [Figs. 12(e) and 12(f), respectively]. Further, the χ'' curve for each composition exhibits a sharp local maximum at temperature $T^{L}_{\chi''} \approx 7.5$ K located slightly below $T^{L}_{\chi'}$. In general, for a ferro-/ferrimagnetic transition, for instance, the onset of the χ'' maximum falls together with the peak maximum of the χ' signal [67]. Further, for NCM811-p the χ' curves do not overlap with each other for different excitation frequencies over the complete measured temper-

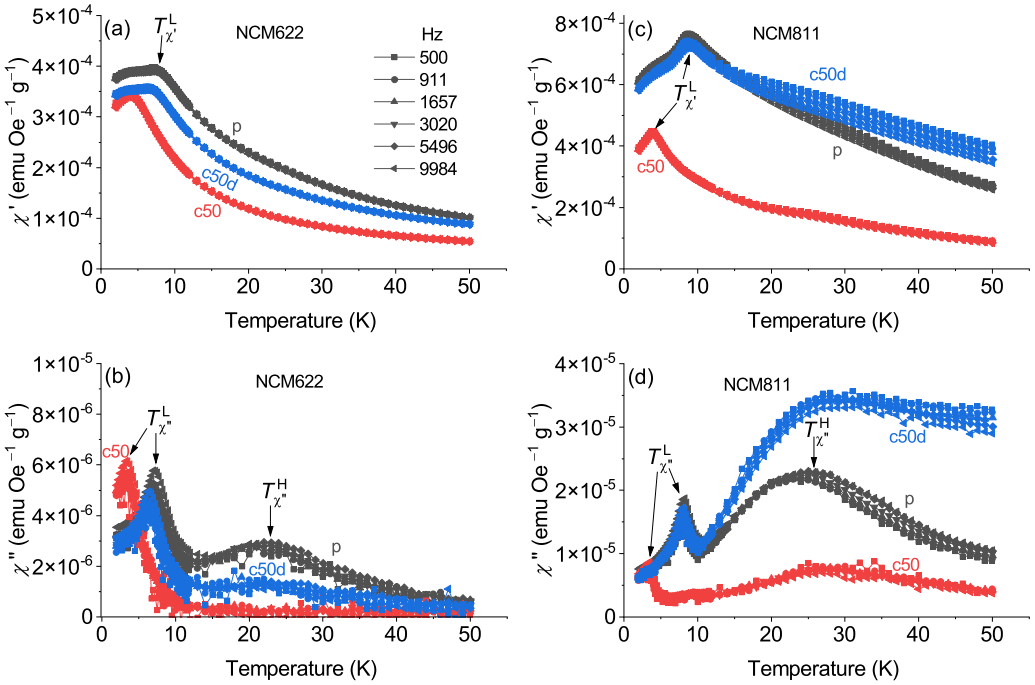

FIG. 13. Measured AC susceptibility vs temperature plots: (a) and (b) χ' and χ'', respectively, at zero DC field, for NCM622 at various states of charge and (c) and (d) χ' and χ'', respectively, for NCM811 at various states of charge. $T^{\mathrm{L}}_{\chi'}$ is the lower temperature of local maximum in the χ' signal. $T^{\mathrm{L}}_{\chi''}$ and $T^{\mathrm{H}}_{\chi''}$ are the low- and high-temperature maxima in the χ'' signal, respectively. Error bars have been omitted for clarity.

ature range 15–50 K, indicating a weak contribution of a (frustrated) ferrimagnetic cluster formation/spin freezing process. This feature of the χ' signal cannot be clearly observed for NCM622-p and NCM111-p. Connected to the nonoverlapping χ' curves of NCM811-p, there is a broad maximum of χ'' located around $T^{\mathrm{H}}_{\chi''} \approx 25$ K that exhibits a relative frequency shift of $\Delta T^{\mathrm{H}}_{\chi''}/[T^{\mathrm{H}}_{\chi''}\Delta(\lg\omega)] \approx 1.5\%$ [Figs. 12(b) and 12(d)]. For NCM622-p, a broad maximum in the χ'' curve is much less pronounced and located around $T^{\mathrm{H}}_{\chi''} \approx 23$ K, and for NCM111-p an even weaker and broad maxima around $T^{\mathrm{H}}_{\chi''} \approx 14$ K can hardly be observed.

The further considerations that also include the delithiated (c50) and relithiated (c50d) samples were restricted to NCM811 and NCM622 material, since for NCM111-p the broad maximum in χ'' is too weak. Figures 13(a) and 13(b) present χ' and χ'', respectively, for NCM622 material in the pristine state (p), delithiated to $x = 0.5$ (c50), and delithiated to $x = 0.5$ and relithiated again to 2.5 V (c50d). For the charged sample NCM622-c50, the local maximum of χ' has shifted from $T^{\mathrm{L}}_{\chi'} \approx 8$ K (NCM622-p) to slightly below 4 K. The low-temperature maximum of χ'' has decreased from $T^{\mathrm{L}}_{\chi''} \approx 7.5$ K for NCM622-p to about 3.5 K for NCM622-c50. Simultaneously, the high-temperature maximum located around $T^{\mathrm{H}}_{\chi''} \approx 23$ K (NCM622-p) is no longer present for NCM622-c50. The relithiated/discharged material NCM622-c50d essentially exhibits very similar features as the pristine NCM622-p material again, but they are not identical, thereby reflecting that discharging cannot fully restore the initial pristine state. For the delithiated/charged sample NCM811-c50, the local maximum of χ' has shifted from $T^{\mathrm{L}}_{\chi'} \approx 9$ K (NCM811-p) to slightly below 4 K and the curves measured at different excitation frequencies now are superimposed with each other compared to the pristine sample [see Figs. 13(c) and 13(d)]. The absolute values of χ' and χ'' for NCM811-c50 have been reduced considerably in general compared with the pristine sample. The low-temperature maximum of χ'' has decreased from $T^{\mathrm{L}}_{\chi''} \approx 8$ K for NCM811-p to about 3.6 K for NCM811-c50. Simultaneously, the high-temperature maximum of χ'' has increased slightly from $T^{\mathrm{H}}_{\chi''} \approx 25$ K for NCM811-p to about 28 K for NCM811-c50, and the absolute values are reduced tremendously as also observed for NCM622. The relithiated/discharged material NCM811-c50d essentially exhibits similar, but not identical, features as the pristine NCM811-p material again pointing to the fact that the initial pristine state cannot fully be restored by discharging again. These results will be discussed together with the results from the other methods below in Sec. IV.

7. *Heat capacity*

Figure 14(a) plots the measured isobaric heat capacity $C_{\mathrm{p}}^{\mathrm{exp}}$ vs temperature curves from 1.8 to 300 K (open symbols) for pristine NCM111-p, NCM622-p, and NCM811-p samples. At 300 K, the Dulong-Petit limit of $3N_{\mathrm{A}}k_{\mathrm{B}} \approx 24.9\,\mathrm{J\,K^{-1}\,mol^{-1}}$ has not been reached yet. The lattice contributions to the isobaric $C_{\mathrm{p}}^{\mathrm{exp}}$ can be expressed as a linear combination of a Debye and an Einstein term [68],

$$C_{\mathrm{p}} \approx C_{\mathrm{p}}^{\mathrm{DE}} = \zeta_{\mathrm{D}}\left[9N_{\mathrm{A}}k_{\mathrm{B}}\left(\frac{T}{T_{\mathrm{D}}}\right)^3\int_0^{T_{\mathrm{D}}/T}\frac{q^4\cdot e^q}{(e^q-1)^2}dq\right] + (1-\zeta_{\mathrm{D}})\left[3N_{\mathrm{A}}k_{\mathrm{B}}\left(\frac{T_{\mathrm{E}}}{T}\right)^2 e^{(-T_{\mathrm{E}}/T)}\right], \quad (2)$$

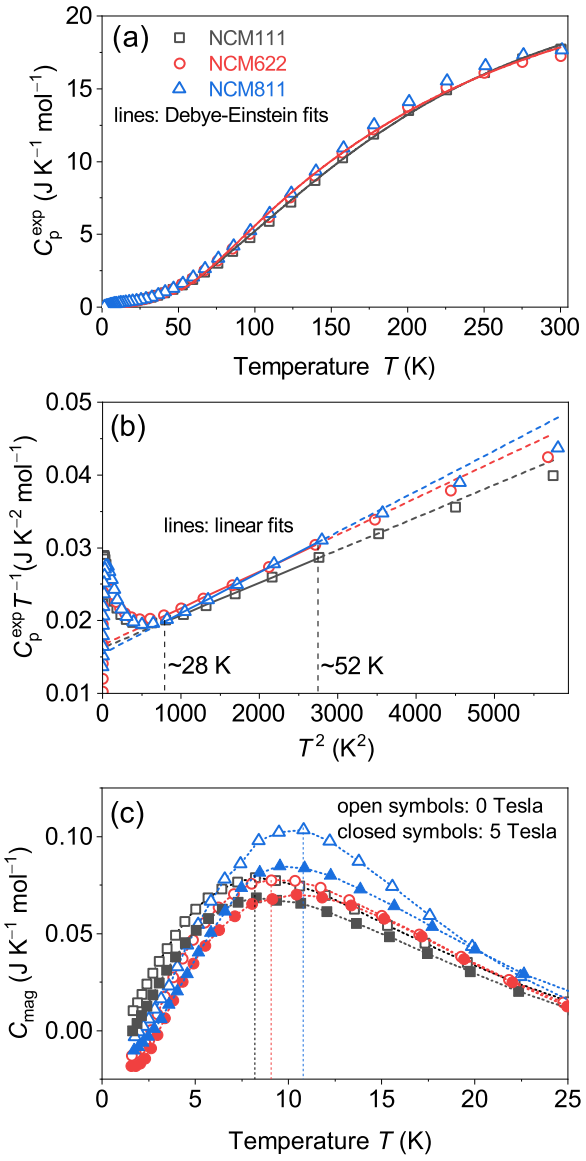

FIG. 14. (a) Measured isobaric heat capacity C_p^{exp} measured for pristine NCM111, NCM622, and NCM811 active material (circles) at zero field together with Debye-Einstein fits (lines) from about 52 to 300 K. The obtained parameters from the fit are listed in Table S6 within the SM [38]. (b) C_p^{exp}/T vs T^2 together with linear fits from ~28 to ~52 K. (c) Difference curves C_{mag} between C_p^{exp} (that has been measured at a magnetic DC field of either zero or 5 Tesla) and the extracted background signal from the linear fit shown in (b).

with Debye contribution parameter ζ_D, Avogadro constant N_A, Boltzmann constant k_B, Debye temperature T_D, and Einstein temperature T_E. These terms only consider the energy contributions from lattice vibrations and do not consider contributions from free electrons or magnetic phase transitions. The Debye and the Einstein terms can be considered to account for acoustic and optic phonons, respectively. Table S6 within the SM [38] lists the ζ_D parameter and the Debye and Einstein temperatures T_D, and T_E, respectively, that have been obtained by fits from about 52 to 300 K to the experimental curves (very low temperatures have been excluded because of contributions from magnetic transitions). Taking the relatively large standard deviations into account, a clear trend of the refined parameters in dependence of the samples' composition cannot be attested. The Debye temperature T_D can also be expressed as a function of the speed of sound v_D, and the molar volume V_M [69],

$$T_D = \frac{\hbar \cdot v_D}{k_B} \left(\frac{6\pi^2 N_A}{V_M} \right)^{1/3}. \quad (3)$$

The molar volume V_M can also expressed as $(1/V_M)^{1/3} = (M_M/\rho)^{1/3}$, with the mass density ρ (obtained from the Rietveld refinements to the XRD data) and the molar mass M_M. Assuming that v_D is the same for all compositions, $T_D \propto (1/V_M)^{1/3}$. As can be inferred from Table S6 within the SM [38], $(1/V_M)^{1/3}$ theoretically increases slightly in the order NCM111-p, NCM-622-p, NCM-811-p, but this trend is very weak. From NCM111-p to NCM-811-p, M_M is slightly increasing, since more of the lighter Mn (54.938 g mol^{-1}) is substituted by the heavier Ni (58.639 g mol^{-1}). On the other side, the mass density ρ is also increasing slightly in this order, compensating partially the molar mass effect on the molar volume V_M. Overall, the effect of sample composition on the heat capacity is too small to be reflected by the refined parameters with relatively large uncertainties. Low temperature heat capacity measurements have been published for the end members $LiCoO_2$ [70–73], $LiNiO_2$ [74], but for NCM materials thermal properties are mostly restricted to room and high temperatures [75–79] that are of high relevance for application.

Figure 14(b) plots C_p^{exp}/T vs T^2 in the low-temperature regime for all pristine materials. The linear region from ≈28 to ≈52 K was used to extract a background signal for the very low-temperature region where a magnetic transition is contributing at about 10 K to the heat-capacity signal. Figure 14(c) shows the magnetic contribution to heat capacity C_{mag}, obtained by subtracting the corresponding background signals from the measured C_p^{exp} curves (that have been measured at a magnetic DC field of either zero or 5 Tesla). In the order NCM111-p, NCM611-p, and NCM811-p, the local maximum of C_{mag} at zero field slightly shifts from 8.0(5) to 9.0(5) to 10.8(5) K, respectively, i.e., at temperatures where DC and AC magnetometry also indicate a magnetic phase transition. A clear shift of the local maxima to a higher (lower) temperatures when a magnetic field of 5 Tesla is applied that would be characteristic for a ferromagnetic (antiferromagnetic) phase transition, respectively, could not be observed here. The ferrimagnetic cluster formation that continuously sets in below about 100 K is smeared out over a broad temperature region and cannot be discriminated from the lattice phonons that contribute much stronger to the heat capacity signal at these elevated temperatures.

IV. SUMMARY AND INTERPRETATION OF RESULTS

The condition for charge neutrality requires the TMs in $Li(TM)O_2$ to be present at an average hypothetical oxidation state of TM^{+3}. It can be observed for the NCM materials, that there is a tendency for the reduction of Ni from Ni^{3+} to Ni^{2+} with a simultaneous oxidation of Mn from Mn^{3+} to Mn^{4+}, together leading to an enhanced effective magnetic moment.

As a rough estimation, for NCM111-p all of the of Ni^{3+} (0.333 per f.u.) could in principle be reduced to Ni^{2+} with simultaneous oxidation of Mn^{3+} to Mn^{4+}, and as a consequence NCM111-p exhibits the largest effective magnetic moment [see Fig. 8(a)] and the lowest-average Ni oxidation state [see Fig. 10(a)], but also the lowest total amount of Ni ions from the series. On the other side, for NCM811-p a smaller total amount of Ni^{3+} (only 0.1 per f.u.) can be reduced with simultaneous oxidation of Mn^{3+} and therefore NCM811-p exhibits the smallest effective magnetic moment, the highest average Ni oxidation state (Ni^{2+}: Ni^{3+} ratio equal 1:7), but also the highest total amount of Ni ions from the series.

Since NCM811-p has the highest ratio of Ni to Co/Mn of this series, the intralayer FM coupling between the Ni ions with each other contributes to an overall FM coupling that is also reflected by the positive Weiss constant θ_{CW} [see Fig. 8(b)]. For NCM622-p and even more pronounced for NCM111-p, the higher amount of Mn leads to a negative Weiss constant, because the intralayer AFM coupling between Ni and Mn comes more and more into play. As a consequence, the magnetization measured at low temperature of 2 K, where the magnetic exchange coupling leads to magnetic order (and/or spin freezing), is higher for NCM811-p at 70 kOe than for NCM622-p or NCM111-p even though the effective magnetic moment is smaller for NCM811-p than for NCM622-p and NCM111-p (see Fig. 6). The comparably large magnetic moments of the Mn^{4+} ions that are present in larger amounts in NCM111, reduce the measured magnetization at low temperature owing to their AFM coupling with the Ni moments.

For the discharged states, there exist two different magnetic transitions/spin freezing events that are located at different temperatures. Firstly, the ferrimagnetic cluster formation at higher temperature will be considered: NCM811-p exhibits a clear broad maximum of χ'' that is centered around about 25 K, whereas for NCM622-p a much weaker broad maximum is centered around about 22 K, and for NCM111-p an even weaker broad maximum is centered around about 14 K (see Fig. 12). These maxima are ascribed to the continuous formation of ferrimagnetic clusters that already sets in below about 100 K as indicated by the ZFC/FC susceptibility curve bifurcations of the discharged samples (Fig. 4). Sow and Kumar [25] investigated how the magnetic characteristics evolve when more and more Li is substituted by Ni for $Li_{1-y}Ni_{1+y}O_2$. They supposed to effectively treat Ni^{2+} as a magnetic impurity in an AFM matrix and found that the concentration of Ni^{2+} decisively changes the magnetic interactions. With increasing substitution of Li by Ni, they found for $Li_{0.98}Ni_{1.02}O_2$, $Li_{0.95}Ni_{1.05}O_2$, $Li_{0.84}Ni_{1.16}O_2$, $Li_{0.68}Ni_{1.32}O_2$ an evolution from spin-glass (SG), to cluster glass (CG), to reentrant spin glass (RSG), and to long-range ferromagnetic (FM) behavior, respectively. A maxima in χ' and χ'' of the AC susceptibility around 12 K has been found for the $Li_{0.98}Ni_{1.02}O_2$ sample with a relative frequency shift that is characteristic for SG and maxima in χ' and χ'' have been found around 30 K for the $Li_{0.95}Ni_{1.05}O_2$ sample with a relative frequency shift that is characteristic for CG. The authors of the present paper interpret a shift of the AC maxima to higher temperature by an increased probability to find more Ni^{2+}/Ni^{3+} in the TM layer in the direct vicinity of a Ni^{2+} in the Li layer that interact with each other via the very strong AFM 180° Ni^{2+}-O-Ni^{2+} and the strong AFM 180° Ni^{2+}-O-Ni^{3+} couplings [11]. The larger the clusters of such a Ni^{2+}/Ni^{3+} accumulation the higher is the temperature of ferrimagnetic ordering of the clusters. It is important to note that for these samples the TM layer is fully occupied by Ni and that additionally some of the Li in the Li layer is substituted by Ni. This substitution reduces the Ni redox state and increases the amount of Ni^{2+}. However, the situation for the NCM materials investigated in this paper has some particular differences. Only the exchange of Li from the Li layer with Ni^{2+} from the TM layer plays a role and no additional Ni by substitution is introduced. Further, the amount of Ni^{2+} in the samples is strongly determined by the samples' composition. Even though a slightly higher occupation of the Li layer by Ni^{2+} has been found for NCM111-p and NCM622-p than for NCM811-p (see η parameter in Fig. 3), the rough probability to find another Ni^{2+}/Ni^{3+} in direct vicinity in the TM layer and to form a cluster becomes strongly reduced from 80 to 60 and to 33.3% in the order NCM811-p, NCM622-p, and NCM111-p. As a consequence, NCM811-p exhibits the strong broad maximum of χ'' that is centered around about 25 K, whereas for NCM111-p only a very weak broad maximum can be detected around about 14 K. The formation of these localized ferrimagnetic clusters could also be considered as a local and low-dimensional (1D) ordering without pronounced long-range correlation.

Whereas the composition strongly affects the temperature where the χ'' maximum is located that is ascribed to ferrimagnetic cluster formation, NCM811-p, NCM622-p, and NCM111-p, all exhibit another magnetic transition slightly below 10 K as indicated by the clear bifurcation between the ZFC and FC curve of the DC susceptibility plots (Fig. 4), by the local maxima of χ' and χ'' of the AC susceptibility curves (Fig. 12), and by the diffuse maximum in the heat capacity measurements (Fig. 14). This low-temperature magnetic transition is considered as a long-range magnetic ordering/spin freezing in three dimensions (3D) referring also to the interpretation of Wikberg *et al.* who investigated a NCM811 sample by muon-spin relaxation/rotation and by DC/AC magnetometry [53,54]. They also report a considerable ZFC/FC bifurcation below about 10 K and accompanying hysteresis in the field scans up to about 40 K. They interpret the data as to have a 3D frustrated system as ground state at 2 K, followed by a transition into a possible 2D spin-glass above 22 K. With further increasing temperature, the compound shows the presence of remaining correlations with increasing effective dimensionality all the way up to the ferrimagnetic transition at 70 K. The fact that NCM811-p, NCM622-p, and NCM111-p, all exhibit the low temperature magnetic transition slightly below 10 K, despite their very different Ni to Mn/Co ratio, points to a comparably weak magnetic coupling path that all compositions have in common and that is capable to magnetically couple the TM layers on a long-range scale and not only locally as for the cluster formation at higher temperature. The weak TM interlayer coupling via the Li layer that is present also without the occupation of the Li layer by TM throughout the whole bulk is suggested to finally cause this frustrated 3D long-range magnetic ordering at low

temperature. Compared to NCM622 and NCM111, the Ni-rich NCM811 exhibits stronger contributions of spin-glass-like characteristics to both magnetic transitions. The reason for that are supposedly the comparably weak 90° Ni^{2+}-O-Ni^{2+} and Ni^{2+}-O-Ni^{3+} FM intralayer couplings that are present at higher density in NCM811 and that allow to have very low-energy excitations to different (frustrated) spin orderings [see also Figs. 1(d)–1(f)]. In contrast, for NCM622 and NCM111 the much stronger 90° Ni^{2+}-O-Mn^{4+} AFM intralayer couplings inhibit quasi-equal-energy states with different spin orderings and, probably even more importantly, the higher Co amount reduces the spin-glass-like characteristics by interrupting the magnetic coupling paths.

By electrochemical charging, Ni^{2+} is oxidized to Ni^{3+} and partially also further to Ni^{4+} (as inferred from the evolution of the effective magnetic moments, and from the XAS and NMR analysis), while the important 180° AFM coupling weakens tremendously in the order Ni^{2+}-O-Ni^{2+}, Ni^{2+}-O-Ni^{3+}, and Ni^{2+}-O-Ni^{4+}. Most clearly, this can be seen for NCM811 (see Fig. 13): The absolute signal strengths of χ' as well as that of χ'' are significantly lower for NCM811-c50 than for NCM811-p, since also the absolute values of the effective magnetic moment is reduced by the charging process (see Fig. 8). More importantly, the broad maximum of the χ'' signal that is located around 25 K for NCM811-p has a strongly reduced integrated intensity for NCM811-c50 (in agreement with the vanished ZFC-FC bifurcation above 10 K), since essential amounts of Ni^{3+} have been oxidized to Ni^{4+} with a heavily reduced AFM interlayer exchange coupling. As a consequence, the ferrimagnetic cluster formation is highly suppressed for the charged samples. For the same reason also the (frustrated) 3D long-range magnetic ordering at temperatures below 10 K are further shifted to even lower temperatures for the charged samples.

V. CONCLUSIONS

The systematic investigation of NCM samples with different Ni to Co/Mn ratios at different states of charge by a broad variety of analytical methods allowed to get new and valuable insights into the correlation between structural details, the TMs' redox states and the magnetic properties. Magnetic parameters as the effective magnetic moment, the Weiss constant that contains information about the "average" magnetic coupling (FM or AFM), and maximum values of magnetization at 2 and 300 K, could qualitatively be understood quite well by the spin-only magnetic moments of the corresponding Ni, Co, and Mn cations in quasi-octahedral coordination that are interacting with each other via the complex magnetic coupling scheme as reported by Chernova *et al.* [11]. Further, especially the AC susceptibility data that has been obtained for different compositions not only for the pristine state but also for the charged and redischarged states, uniquely allow to discriminate a low-dimensional short-range from a (frustrated) 3D long-range magnetic transition/spin freezing occurring at higher and lower temperatures, respectively, and to evaluate their spin-glass like characteristics. Elaboration of the magnetic contributions to the heat-capacity signal for the pristine state essentially supported the hypothesis of a (frustrated) 3D long-range magnetic transition at low temperature. The results from AC susceptibility are also well reflected by the detailed ZFC/FC bifurcation behavior of the DC susceptibility data.

For an even deeper understanding of the magnetic transitions/spin freezing transitions in these layered oxides beyond what has been inferred in this paper, the Ni/Co/Mn cationic short-range arrangements in close vicinity to the migrated interslab Ni^{2+} ions would be needed to be analyzed in more detail in addition to the Li/Ni site disorder. This challenge could be tackled by a combination of NMR and neutron diffraction for instance, ideally for a variety of compositions with differently adjusted Li/Ni disorders at various states of charge.

VI. EXPERIMENTAL

The experimental details can be found in Sec. S2 within the SM [38] (including Refs. [11,80–84]).

ACKNOWLEDGMENTS

We thank Dr. Marcus Müller from the electrode development group at the Institute for Applied Materials-Energy Storage Systems (IAM-ESS) at KIT for providing the pristine NCM layered oxides from industrial manufacturers. We acknowledge Dr. Thomas Bergfeldt from the chemical analytics group at the Institute for Applied Materials-Applied Materials Physics (IAM-AWP) at KIT for the quantitative ICP-OES and CGHE analysis. This work contributes to the research performed at CELEST (Center for Electrochemical Energy Storage Ulm-Karlsruhe).

DATA AVAILABILITY

The data are not publicly available. The data are available from the authors upon reasonable request.

[1] N. Nitta, F. Wu, J. T. Lee, and G. Yushin, Li-ion battery materials: Present and future, Mater. Today **18**, 252 (2015).

[2] A. Manthiram, A reflection on lithium-ion battery cathode chemistry, Nat. Commun. **11**, 1550 (2020).

[3] T. Kim, W. Song, D.-Y. Son, L. K. Ono, and Y. Qi, Lithium-ion batteries: Outlook on present, future, and hybridized technologies, J. Mater. Chem. A **7**, 2942 (2019).

[4] L. Britala, M. Marinaro, and G. Kucinskis, A review of the degradation mechanisms of NCM cathodes and corresponding mitigation strategies, J. Energy Storage **73**, 108875 (2023).

[5] M. Malik, K. H. Chan, and G. Azimi, Layered $Li_xNi_yMn_yCo_{1-2y}O_2$ cathodes for lithium ion batteries: Understanding local structure via magnetic properties, Mater. Today Energy **28**, 101066 (2022).

[6] A. Chakraborty, S. Kunnikuruvan, M. Dixit, and D. T. Major, Review of computational studies of NCM cathode materials for Li-ion batteries, Isr. J. Chem. **60**, 850 (2020).

[7] D. Goonetilleke, B. Schwarz, H. Li, F. Fauth, E. Suard, S. Mangold, S. Indris, T. Brezesinski, M. Bianchini, and D. Weber, Stoichiometry matters: Correlation between antisite defects, microstructure and magnetic behavior in the cathode material $Li_{1-z}Ni_{1+z}O_2$, J. Mater. Chem. A **11**, 13468 (2023).

[8] H. Li, W. Hua, B. Schwarz, M. Etter, S. Mangold, G. Melinte, N. P. M. Casati, H. Ehrenberg, and S. Indris, Investigation of structural and electronic changes induced by postsynthesis thermal treatment of $LiNiO_2$, Chem. Mater. **34**, 8163 (2022).

[9] H. Li, W. Hua, X. Liu-Théato, Q. Fu, M. Desmau, A. Missyul, M. Knapp, H. Ehrenberg, and S. Indris, New insights into lithium hopping and ordering in $LiNiO_2$ cathodes during Li (De)intercalation, Chem. Mater. **33**, 9546 (2021).

[10] N. A. Chernova, G. M. Nolis, F. O. Omenya, H. Zhou, Z. Li, and M. S. Whittingham, What can we learn about battery materials from their magnetic properties? J. Mater. Chem. **21**, 9865 (2011).

[11] N. A. Chernova, M. Ma, J. Xiao, M. S. Whittingham, J. Breger, and C. P. Grey, Layered $Li_xNi_yMn_yCo_{1-2y}O_2$ cathodes for lithium ion batteries: Understanding local structure via magnetic properties, Chem. Mater. **19**, 4682 (2007).

[12] A. Abdel-Ghany, A. Mauger, F. Gendron, K. Zaghib, and C. Julien, Magnetic properties of $LiNi_{0.33}Mn_{0.33}Co_{0.33}O_2$ as positive electrode for Li-Ion batteries, ECS Transactions **3**, 137 (2007).

[13] M. Månsson, H. Nozaki, J. M. Wikberg, K. Prša, Y. Sassa, M. Dahbi, K. Kamazawa, K. Sedlak, I. Watanabe, and J. Sugiyama, Lithium diffusion & magnetism in battery cathode material $Li_xNi_{1/3}Co_{1/3}Mn_{1/3}O_2$, J. Phys.: Conf. Ser. **551**, 012037 (2014).

[14] A. Mauger, F. Gendron, and C. M. Julien, Magnetic properties of $Li_xNi_yMn_yCo_{1-2y}O_2 (0.2 \leqslant 1-2y \leqslant 0.5, 0 \leqslant x \leqslant 1)$, J. Alloys Compd. **520**, 42 (2012).

[15] N. Kızıltaş-Yavuz, M. Herklotz, A. M. Hashem, H. M. Abuzeid, B. Schwarz, H. Ehrenberg, A. Mauger, and C. M. Julien, Synthesis, structural, magnetic and electrochemical properties of $LiNi_{1/3}Mn_{1/3}Co_{1/3}O_2$ prepared by a sol–gel method using table sugar as chelating agent, Electrochim. Acta **113**, 313 (2013).

[16] X.-H. Shi, Y.-P. Wang, X. Cao, S. Wu, Z. Hou, and Z. Zhu, Charge compensation mechanisms and oxygen vacancy formations in $LiNi_{1/3}Mn_{1/3}Co_{1/3}O_2$: First-principles calculations, ACS Omega **7**, 14875 (2022).

[17] X. Zhang, A. Mauger, Q. Lu, H. Groult, L. Perrigaud, F. Gendron, and C. Julien, Synthesis and characterization of $LiNi_{1/3}Mn_{1/3}Co_{1/3}O_2$ by wet-chemical method, Electrochim. Acta **55**, 6440 (2010).

[18] X. Zhang, C. M. Julien, A. Mauger, and F. Gendron, Magnetic analysis of lamellar oxides for Li-ions batteries, Solid State Ionics **188**, 148 (2011).

[19] E. Chappel, M. D. Núñez-Regueiro, S. de Brion, G. Chouteau, V. Bianchi, D. Caurant, and N. Baffier, Interlayer magnetic frustration in quasistoichiometric $Li_{1-x}Ni_{1+x}O_2$, Phys. Rev. B **66**, 132412 (2002).

[20] M. Holzapfel, S. de Brion, C. Darie, P. Bordet, E. Chappel, G. Chouteau, P. Strobel, A. Sulpice, and M. D. Núñez-Regueiro, Decoupling of orbital and spin degrees of freedom in $Li_{1-x}Na_xNiO_2$, Phys. Rev. B **70**, 132410 (2004).

[21] K. Mukai, J. Sugiyama, Y. Ikedo, Y. Aoki, D. Andreica, and A. Amato, Structural and magnetic nature for fully delithiated Li_xNiO_2: Comparative study between chemically and electrochemically prepared samples, J. Phys. Chem. C **114**, 8626 (2010).

[22] M. Núnez-Regueiro, E. Chappel, G. Chouteau, and C. Delmas, Magnetic structure of $Li_{1-x}Ni_{1+x}O_2$, Eur. Phys. J. B **16**, 37 (2000).

[23] P. Ganguly, V. Ramaswamy, I. S. Mulla, R. F. Shinde, P. P. Bakare, S. Ganapathy, P. R. Rajamohanan, and N. V. K. Prakash, Application of a layered triangular-lattice magnetic model system to $LiNiO_2$, Phys. Rev. B **46**, 11595 (1992).

[24] F. Reynaud, D. Mertz, F. Celestini, J.-M. Debierre, A. M. Ghorayeb, P. Simon, A. Stepanov, J. Voiron, and C. Delmas, Orbital frustration at the origin of the magnetic behavior in $LiNiO_2$, Phys. Rev. Lett. **86**, 3638 (2001).

[25] C. Sow and P. S. Anil Kumar, Evolution of ferromagnetism from a frustrated state in $Li_xNi_{(2-x)}O_2$ $(0.67 < x < 0.98)$, J. Phys.: Condens. Matter **25**, 496001 (2013).

[26] K. Yamaura, M. Takano, A. Hirano, and R. Kanno, Magnetic Properties of $Li_{1-x}Ni_{1+x}O_2$ $(0 \lesssim x \lesssim 0.08)$, J. Solid State Chem. **127**, 109 (1996).

[27] P. Anderson, Resonating valence bonds: A new kind of insulator? Mater. Res. Bull. **8**, 153 (1973).

[28] G. H. Wannier, Antiferromagnetism. The triangular ising net, Phys. Rev. **79**, 357 (1950).

[29] K. Hirakawa, H. Kadowaki, and K. Ubukoshi, Experimental studies of triangular lattice antiferromagnets with $S = 1/2$: $NaTiO_2$ and $LiNiO_2$, J. Phys. Soc. Jpn. **54**, 3526 (1985).

[30] K. Hirakawa, R. Osborn, A. D. Taylor, and K. Takeda, Neutron inelastic scattering study of $LiNiO_2$: A Candidate for the spin quantum liquid, J. Phys. Soc. Jpn. **59**, 3081 (1990).

[31] A. P. Ramirez, Strongly geometrically frustrated magnets, Annu. Rev. Mater. Sci. **24**, 453 (1994).

[32] P. W. Anderson, Antiferromagnetism. Theory of superexchange interaction, Phys. Rev. **79**, 350 (1950).

[33] J. B. Goodenough, Theory of the role of covalence in the perovskite-type manganites [La, M(II)]MnO_3, Phys. Rev. **100**, 564 (1955).

[34] J. Kanamori, Theory of the magnetic properties of ferrous and cobaltous oxides, I, Prog. Theor. Phys. **17**, 177 (1957).

[35] J. B. Goodenough, An interpretation of the magnetic properties of the perovskite-type mixed crystals $La_{1-x}Sr_xCoO_{3-\lambda}$, J. Phys. Chem. Solids **6**, 287 (1958).

[36] J. Kanamori, Superexchange interaction and symmetry properties of electron orbitals, J. Phys. Chem. Solids **10**, 87 (1959).

[37] J. Kanamori, Crystal distortion in magnetic compounds, J. Appl. Phys. **31**, S14 (1960).

[38] See Supplemental Material at http://link.aps.org/supplemental/10.1103/PhysRevMaterials.9.045401 for additional (i) Secs. S1: Calculation of magnetic energy for specific cationic arrangements; S2: Experimental description; (ii) Tables S1: Magnetic exchange coupling constants J_{iso}, S2: Sample production companies, S3: ICP-OES results, S4: EC parameters, S5: Electronic/magnetic parameters for Ni, Co, and Mn, S6: Heat capacity parameters, S7: Which sample has been measured by which method, S7: Samples masses; and (iii) Figs. S1–S3: EC charging/discharging curves, S4–S6: Rietveld refinements to XRD patterns, S8: Inverse susceptibility vs temperature curves, S9: Fieldscans at 300 K, S10–S12: Curie-Weiss fits, S13–S15: XAS spectra, S16: Ni K-edge comparison pristine states, S17 to

S19: Fourier transforms of EXAFS oscillations, S20: Diamagnetic corrections.

[39] J. Zheng, G. Teng, C. Xin, Z. Zhuo, J. Liu, Q. Li, Z. Hu, M. Xu, S. Yan, W. Yang, and F. Pan, Role of superexchange interaction on tuning of Ni/Li disordering in layered $Li(Ni_xMn_yCo_z)O_2$, J. Phys. Chem. Lett. **8**, 5537 (2017).

[40] T. Ye, Z. Li, H. Yan, Y. Ha, D. Zhang, C. Zhou, L. Wang, L. Li, and Q. Xiang, Magnetic frustration effect on the rate performance of $LiNi_{0.6}Co_{0.4-x}Mn_xO_2$ cathodes for lithium-ion batteries, Adv. Energy Mater. **12**, 2201556 (2022).

[41] B. Schwarz and Q. Fu, Magnetic single-ion anisotropy and Curie-Weiss behaviour of $Mg_3v_4(PO_4)_6$, Eur. J. Inorg. Chem. **27**, e202400162 (2024).

[42] H. M. Rietveld, Line profiles of neutron powder-diffraction peaks for structure refinement, Acta Crystallogr. **22**, 151 (1967).

[43] M. I. Aroyo, ed., *International Tables for Crystallography. Space-Group Symmetry*, 6th ed. (Wiley, Chichester, 2016), Vol. A.

[44] L. Azhari, X. Zhou, B. Sousa, Z. Yang, G. Gao, and Y. Wang, Effects of extended aqueous processing on structure, chemistry, and performance of polycrystalline $LiNi_xMn_yCo_zO_2$ cathode powders, ACS Appl. Mater. Interfaces **12**, 57963 (2020).

[45] K. Kleiner, C. A. Murray, C. Grosu, B. Ying, M. Winter, P. Nagel, S. Schuppler, and M. Merz, On the origin of reversible and irreversible reactions in $LiNi_xCo_{(1-x)/2}Mn_{(1-x)/2}O_2$, J. Electrochem. Soc. **168**, 120533 (2021).

[46] L. de Biasi, B. Schwarz, T. Brezesinski, P. Hartmann, J. Janek, and H. Ehrenberg, Chemical, structural, and electronic aspects of formation and degradation behavior on different length scales of Ni-Rich NCM and Li-Rich HE-NCM cathode materials in Li-Ion batteries, Adv. Mater. **31**, 1900985 (2019).

[47] M. J. W. Ogley, A. S. Menon, G. C. Pandey, G. J. Páez Fajardo, B. J. Johnston, I. McClelland, V. Majherova, S. Huband, D. Tripathy, I. Temprano *et al.*, Metal-ligand redox in layered oxide cathodes for Li-ion batteries, Joule **9**, 101775 (2025).

[48] C. Xu, K. Märker, J. Lee, A. Mahadevegowda, P. J. Reeves, S. J. Day, M. F. Groh, S. P. Emge, C. Ducati, B. Layla Mehdi *et al.*, Bulk fatigue induced by surface reconstruction in layered Ni-rich cathodes for Li-ion batteries, Nat. Mater. **20**, 84 (2021).

[49] F. Lin, D. Nordlund, I. M. Markus, T.-C. Weng, H. L. Xin, and M. M. Doeff, Profiling the nanoscale gradient in stoichiometric layered cathode particles for lithium-ion batteries, Energy Environ. Sci. **7**, 3077 (2014).

[50] F. Lin, I. M. Markus, D. Nordlund, T.-C. Weng, M. D. Asta, H. L. Xin, and M. M. Doeff, Surface reconstruction and chemical evolution of stoichiometric layered cathode materials for lithium-ion batteries, Nat. Commun. **5**, 3529 (2014).

[51] P. Xiao, T. Shi, W. Huang, and G. Ceder, Understanding surface densified phases in Ni-rich layered compounds, ACS Energy Lett. **4**, 811 (2019).

[52] T. Moriya, Anisotropic superexchange interaction and weak ferromagnetism, Phys. Rev. **120**, 91 (1960).

[53] J. M. Wikberg, M. Dahbi, I. Saadoune, T. Gustafsson, K. Edström, and P. Svedlindh, Magnetic order, aging, and spin frustration in a percolating spin system, $LiNi_{0.8}Co_{0.1}Mn_{0.1}O_2$, J. Appl. Phys. **108**, 083909 (2010).

[54] J. M. Wikberg, M. Månsson, M. Dahbi, K. Kamazawa, and J. Sugiyama, Magnetic order and frustrated dynamics in $Li(Ni_{0.8}Co_{0.1}Mn_{0.1})O_2$: A study by μ^+ SR and SQUID magnetometry, Phys. Procedia **30**, 202 (2012).

[55] M. Merz, B. Ying, P. Nagel, S. Schuppler, and K. Kleiner, Reversible and irreversible redox processes in Li-rich layered oxides, Chem. Mater. **33**, 9534 (2021).

[56] Y. Zuo, H. Shang, J. Hao, J. Song, F. Ning, K. Zhang, L. He, and D. Xia, Regulating the potential of anion redox to reduce the voltage hysteresis of Li-rich cathode materials, J. Am. Chem. Soc. **145**, 5174 (2023).

[57] C. P. Grey and N. Dupré, NMR studies of cathode materials for lithium-ion rechargeable batteries, Chem. Rev. **104**, 4493 (2004).

[58] O. Pecher, J. Carretero-González, K. J. Griffith, and C. P. Grey, Materials' methods: NMR in battery research, Chem. Mater. **29**, 213 (2017).

[59] D. Zeng, J. Cabana, J. Bréger, W.-S. Yoon, and C. P. Grey, Cation ordering in $Li[Ni_xMn_xCo_{(1-2x)}]O_2$-layered cathode materials: A nuclear magnetic resonance (NMR), pair distribution function, x-ray absorption spectroscopy, and electrochemical study, Chem. Mater. **19**, 6277 (2007).

[60] A. R. Genreith-Schriever, A. Alexiu, G. S. Phillips, C. S. Coates, L. A. V. Nagle-Cocco, J. D. Bocarsly, F. N. Sayed, S. E. Dutton, and C. P. Grey, Jahn–Teller distortions and phase transitions in $LiNiO_2$: Insights from *ab initio* molecular dynamics and variable-temperature x-ray diffraction, Chem. Mater. **36**, 2289 (2024).

[61] A. R. Genreith-Schriever, C. S. Coates, K. Märker, I. D. Seymour, E. N. Bassey, and C. P. Grey, Probing Jahn-Teller distortions and antisite defects in $LiNiO_2$ with ^{7}Li NMR spectroscopy and density functional theory, Chem. Mater. **36**, 4226 (2024).

[62] W.-S. Yoon, C. P. Grey, M. Balasubramanian, X.-Q. Yang, D. A. Fischer, and J. McBreen, Combined NMR and XAS study on local environments and electronic structures of electrochemically Li-Ion deintercalated $Li_{1-x}Co_{1/3}Ni_{1/3}Mn_{1/3}O_2$ electrode system, Electrochem. Solid-State Lett. **7**, A53 (2004).

[63] K. Märker, P. J. Reeves, C. Xu, K. J. Griffith, and C. P. Grey, Evolution of structure and lithium dynamics in $LiNi_{0.8}Mn_{0.1}Co_{0.1}O_2$ (NMC811) Cathodes during electrochemical cycling, Chem. Mater. **31**, 2545 (2019).

[64] A. Grenier, P. J. Reeves, H. Liu, I. D. Seymour, K. Märker, K. M. Wiaderek, P. J. Chupas, C. P. Grey, and K. W. Chapman, Intrinsic kinetic limitations in substituted lithium-layered transition-metal oxide electrodes, J. Am. Chem. Soc. **142**, 7001 (2020).

[65] C. Xu, A. J. Merryweather, S. S. Pandurangi, Z. Lun, D. S. Hall, V. S. Deshpande, N. A. Fleck, C. Schnedermann, A. Rao, and C. P. Grey, Operando visualization of kinetically induced lithium heterogeneities in single-particle layered Ni-rich cathodes, Joule **6**, 2535 (2022).

[66] J. A. Mydosh, *Spin Glasses: An Experimental Introduction*, online-edition, EBL-Schweitzer (CRC Press, Florence, 1993).

[67] M. Bałanda, AC susceptibility studies of phase transitions and magnetic relaxation: Conventional, molecular and low-dimensional magnets, Acta Phys. Pol. A **124**, 964 (2013).

[68] E. S. R. Gopal, *Specific Heats at Low Temperatures* (Springer, New York, 1966).

[69] C. Kittel, *Einführung in die Festkörperphysik* (De Gruyter, Oldenbourg, 2013).

[70] H. Kawaji, M. Takematsu, T. Tojo, T. Atake, A. Hirano, and R. Kanno, Low temperature heat capacity and thermodynamic functions of $LiCoO_2$, J. Therm. Anal. Calorim. **68**, 833 (2002).

[71] P. Gotcu-Freis, D. M. Cupid, M. Rohde, and H. J. Seifert, New experimental heat capacity and enthalpy of formation of lithium cobalt oxide, J. Chem. Thermodyn. **84**, 118 (2015).

[72] M. Menetrier, D. Carlier, M. Blangero, and C. Delmas, On "Really" stoichiometric $LiCoO_2$, Electrochem. Solid-State Lett. **11**, A179 (2008).

[73] A. L. Emelina, M. A. Bykov, M. L. Kovba, B. M. Senyavin, and E. V. Golubina, Thermochemical properties of lithium cobaltate, Russ. J. Phys. Chem. A **85**, 357 (2011).

[74] H. Kawaji, T. Oka, T. Tojo, T. Atake, A. Hirano, and R. Kanno, Low-temperature heat capacity of layer structure lithium nickel oxide, Solid State Ionics **152-153**, 195 (2002).

[75] P. Bohn, G. Liebig, L. Komsiyska, and G. Wittstock, Temperature propagation in prismatic lithium-ion-cells after short term thermal stress, J. Power Sources **313**, 30 (2016).

[76] A. Loges, S. Herberger, P. Seegert, and T. Wetzel, A study on specific heat capacities of Li-ion cell components and their influence on thermal management, J. Power Sources **336**, 341 (2016).

[77] M. Steinhardt, J. V. Barreras, H. Ruan, B. Wu, G. J. Offer, and A. Jossen, Meta-analysis of experimental results for heat capacity and thermal conductivity in lithium-ion batteries: A critical review, J. Power Sources **522**, 230829 (2022).

[78] G. Liebig, U. Kirstein, S. Geißendörfer, O. Zahid, F. Schuldt, and C. Agert, The impact of environmental factors on the thermal characteristic of a lithium–ion battery, Batteries **6**, 3 (2020).

[79] P. Gotcu, W. Pfleging, P. Smyrek, and H. J. Seifert, Thermal behaviour of Li_xMeO_2 (Me = Co or Ni + Mn + Co) cathode materials, Phys. Chem. Chem. Phys. **19**, 11920 (2017).

[80] L. W. Finger, D. E. Cox, and A. P. Jephcoat, A correction for powder diffraction peak asymmetry due to axial divergence, J. Appl. Crystallogr. **27**, 892 (1994).

[81] J. Rodríguez-Carvajal, Recent advances in magnetic structure determination by neutron powder diffraction, Phys. B: Condens. Matter **192**, 55 (1993).

[82] Y. Xiao, T. Liu, J. Liu, L. He, J. Chen, J. Zhang, P. Luo, H. Lu, R. Wang, W. Zhu *et al.*, Insight into the origin of lithium/nickel ions exchange in layered $Li(Ni_xMn_yCo_z)O_2$ cathode materials, Nano Energy **49**, 77 (2018).

[83] J. F. Berar and P. Lelann, ESD's and estimated probable error obtained in Rietveld refinements with local correlations, J. Appl. Crystallogr. **24**, 1 (1991).

[84] K. M. Padden, J. F. Krebs, C. E. MacBeth, R. C. Scarrow, and A. S. Borovik, Immobilized metal complexes in porous organic hosts: Development of a material for the selective and reversible binding of nitric oxide, J. Am. Chem. Soc. **123**, 1072 (2001).